THE JOURNAL OF BIOLOGICAL CHEMISTRY VOL. 292, NO. 1, pp. 64–79, January 6, 2017

Phosphorylation of Cytochrome *c* Threonine 28 Regulates Electron Transport Chain Activity in Kidney

IMPLICATIONS FOR AMP KINASE[*][S]

Received for publication, June 22, 2016, and in revised form, September 20, 2016 Published, JBC Papers in Press, October 7, 2016, DOI 10.1074/jbc.M116.744664

Gargi Mahapatra,[a,b] Ashwathy Varughese,[a,b] Qinqin Ji,[c] Icksoo Lee,[a,d] Jenney Liu,[a] Asmita Vaishnav,[b] Christopher Sinkler,[a] Alexandr A. Kapralov,[e] Carlos T. Moraes,[f] Thomas H. Sanderson,[g] Timothy L. Stemmler,[h] Lawrence I. Grossman,[a] Valerian E. Kagan,[e] Joseph S. Brunzelle,[i] Arthur R. Salomon,[j] Brian F. P. Edwards,[b] and Maik Hüttemann[a,b1]

From the [a]Center for Molecular Medicine and Genetics and the Departments of [b]Biochemistry and Molecular Biology, [g]Emergency Medicine, and [h]Pharmaceutical Sciences, Wayne State University, Detroit, Michigan 48201, the [c]Chemistry Department and the [j]MCB Department, Brown University, Providence, Rhode Island 02912, the [d]College of Medicine, Dankook University, Cheonan-si, Chungcheongnam-do 31116, Republic of Korea, the [e]Center for Free Radical and Antioxidant Health and the Department of Environmental and Occupational Health, University of Pittsburgh, Pittsburgh, Pennsylvania 15219, the [f]Department of Neurology, University of Miami School of Medicine, Miami, Florida 33136, and the [i]Life Sciences Collaborative Access Team, Northwestern University, Center for Synchrotron Research, Argonne, Illinois 60439

Edited by Dennis R. Voelker

Mammalian cytochrome *c* (Cyt*c*) plays a key role in cellular life and death decisions, functioning as an electron carrier in the electron transport chain and as a trigger of apoptosis when released from the mitochondria. However, its regulation is not well understood. We show that the major fraction of Cyt*c* isolated from kidneys is phosphorylated on Thr^{28}, leading to a partial inhibition of respiration in the reaction with cytochrome *c* oxidase. To further study the effect of Cyt*c* phosphorylation *in vitro*, we generated T28E phosphomimetic Cyt*c*, revealing superior behavior regarding protein stability and its ability to degrade reactive oxygen species compared with wild-type unphosphorylated Cyt*c*. Introduction of T28E phosphomimetic Cyt*c* into Cyt*c* knock-out cells shows that intact cell respiration, mitochondrial membrane potential ($\Delta\Psi_m$), and ROS levels are reduced compared with wild type. As we show by high resolution crystallography of wild-type and T28E Cyt*c* in combination with molecular dynamics simulations, Thr^{28} is located at a central position near the heme crevice, the most flexible epitope of the protein apart from the N and C termini. Finally, *in silico* prediction and our experimental data suggest that AMP kinase, which phosphorylates Cyt*c* on Thr^{28} *in vitro* and colocalizes with Cyt*c* to the mitochondrial intermembrane space in the kidney, is the most likely candidate to phosphorylate Thr^{28} *in vivo*. We conclude that Cyt*c* phosphorylation is mediated in a tissue-specific manner and leads to regulation of electron transport chain flux via "controlled respiration," preventing $\Delta\Psi_m$ hyperpolarization, a known cause of ROS and trigger of apoptosis.

Cytochrome *c* (Cyt*c*)[2] is a small (12-kDa) globular nucleus-encoded mitochondrial protein containing a covalently attached heme group with multiple functions. In the electron transport chain (ETC), it functions as a single electron carrier between bc_1 complex (complex III) and cytochrome *c* oxidase (*Cc*O, complex IV) and is thus essential for aerobic energy production. The second important role of Cyt*c* is seen under conditions of stress, when it functions as a crucial pro-apoptotic signal (1). During apoptosis, Cyt*c* is released from mitochondria into the cytosol, where it interacts with Apaf-1 to form the apoptosome, which in turn activates caspase-9 and the downstream executioner caspase cascade. Furthermore, Cyt*c* functions as a cardiolipin peroxidase during the early phase of apoptosis, when it oxidizes the mitochondrial membrane lipid cardiolipin, thereby facilitating its own release from the inner mitochondrial membrane (2). In contrast, under healthy, non-apoptotic conditions, Cyt*c* acts as a scavenger of reactive oxygen species (ROS) (3), and it takes part in other redox reactions inside mitochondria, including redox-coupled protein import (4) and reduction of p66Shc, a protein that is implicated in the generation of ROS and apoptosis (5).

Given the multiple functions of Cyt*c*, it is not surprising that it is tightly regulated. Two regulatory mechanisms via expression of a somatic and testis-specific isoform pair and allosteric regulation through binding of ATP have been known for over 30 years (6, 7). A third mechanism via reversible phosphorylation was discovered recently when we purified bovine Cyt*c* from heart and liver tissue under conditions preserving the physiological phosphorylation status. The two proteins were phosphorylated on Tyr^{97} and Tyr^{48}, respectively (8, 9). Both

* This work was supported by National Institutes of Health Grants R01 GM089900, R01 NS091242, and T32 HL120822. The authors declare that they have no conflicts of interest with the contents of this article. The content is solely the responsibility of the authors and does not necessarily represent the official views of the National Institutes of Health.

[S] This article contains supplemental Table 1 and Figs. 1–4.

[1] To whom correspondence should be addressed: Center for Molecular Medicine and Genetics, Wayne State University, Detroit, MI 48201. Tel.: 313-577-9150; Fax: 313-577-5218; E-mail: mhuttema@med.wayne.edu.

[2] The abbreviations used are: Cyt*c*, cytochrome *c*; ETC, electron transport chain; *Cc*O, cytochrome *c* oxidase; ROS, reactive oxygen species; AMPK, AMP-activated kinase; CL, cardiolipin; TOCL, tetralinoleyl-CL; PDB, Protein Data Bank; RMSF, root mean square fluctuation(s); Tricine, *N*-[2-hydroxy-1,1-bis(hydroxymethyl)ethyl]glycine; DCIP, 2,6-dichloroindophenol; $\Delta\Psi_m$, mitochondrial membrane potential; ESI, electrospray ionization.

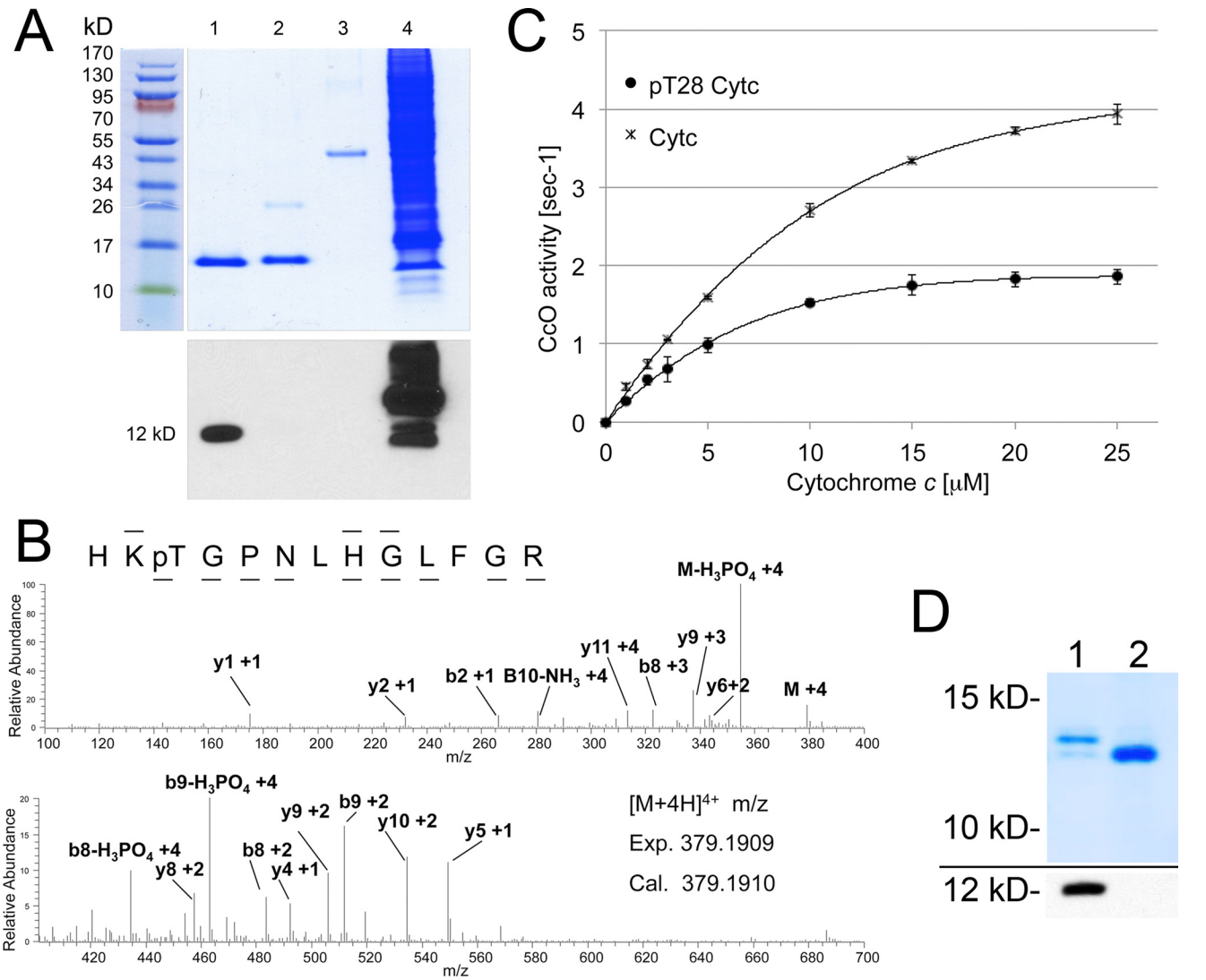

FIGURE 1. **Kidney cytochrome *c* is phosphorylated on threonine 28, leading to controlled respiration.** *A*, purification of cow kidney Cyt*c* indicates threonine phosphorylation. *Lane 1*, kidney Cyt*c*; *lane 2*, cow heart Cyt*c* (Sigma); *lane 3*, ovalbumin (Western negative control); *lane 4*, EGF-treated A431 total cell lysate (Western blotting positive control). *Top*, Coomassie gel; *bottom*, anti-phospho-Thr Western blot. *B*, nano-LC/ESI/MS/MS spectrum of HKpTGPNLHGLFGR reveals phosphorylation of Thr[28]. The phosphorylation site was unambiguously assigned by fragment ions y10 and y11. The sequence of the peptide was assigned by b2, b8, b9, y1, y2, y4, y5, y6, y8, y9, and y10. *C*, *in vitro* cytochrome *c* oxidase activity with *in vivo* phosphorylated Thr[28] (*pT28*) is 50% reduced at maximal turnover compared with unphosphorylated Cyt*c*. *D*, *top*, high resolution gel electrophoresis indicates that 83% of the Cyt*c* pool is phosphorylated (*lane 1*, *top band*); *bottom band*, unphosphorylated Cyt*c*. *Lane 2*, nonspecific phosphatase treatment of Cyt*c* collapses the top band. *Bottom*, Western blotting with an anti-phosphothreonine antibody indicates dephosphorylation of Cyt*c* in *lane 2*. *Error bars*, S.D.

modifications lead to a partial inhibition of respiration. In addition, the phosphomimetic Y48E substitution abolished the capability of Cyt*c* to trigger apoptosis, suggesting that Cyt*c* phosphorylation regulates apoptosis at the level of the apoptosome (10).

Here we report that Cyt*c* purified from bovine and rat kidney tissues in the presence of phosphatase inhibitors is phosphorylated on Thr[28]. *In vivo* phosphorylated and T28E phosphomimetic Cyt*c* led to an inhibition of respiration in the reaction with C*c*O. Introduction of WT and T28E phosphomimetic Cyt*c* into Cyt*c* knock-out cells showed that intact cell respiration, mitochondrial membrane potential ($\Delta\Psi_m$), and ROS levels were reduced. This suggests that Cyt*c* phosphorylation can regulate ETC flux, preventing $\Delta\Psi_m$ hyperpolarization, a known trigger of ROS production and apoptosis (11). Finally, we provide evidence suggesting that phosphorylation of Thr[28] is mediated by AMP kinase (AMPK), which co-localizes with Cyt*c* in the mitochondrial intermembrane space. This is the first report of a mapped phosphorylation site on a mammalian oxidative phosphorylation component, together with functional and structural analyses and a kinase candidate mediating this site-specific modification.

Results

Mammalian Kidney Cytochrome c Is Phosphorylated on Thr[28], Leading to "Controlled Respiration"—To test whether Cyt*c* phosphorylation occurs in mammalian tissues other than the heart and liver, where it is tyrosine-phosphorylated, we chose the kidney, an organ with a high mitochondrial capacity and the second highest oxygen consumption rate only after heart (12). Surprisingly, Western blotting analysis of Cyt*c* from bovine kidney detected phosphorylation on threonine (Fig. 1*A*)

but not on tyrosine (not shown). Mass spectrometry unambiguously revealed that Thr[28] was phosphorylated in three independent Cyt*c* isolations analyzed (Fig. 1*B*). This amino acid is conserved in mammals, both in the somatic and testes-specific isoform (supplemental Fig. 1*A*). To test the effect of Thr[28] phosphorylation, we measured the kinetics of *in vivo* phosphorylated Cyt*c* with isolated C*c*O. Oxygen consumption was 50% lower at maximal turnover for Thr[28]-phosphorylated *versus* unphosphorylated Cyt*c* (Fig. 1*C*). Phosphorylation of Thr[28] also dropped the apparent K_m of Cyt*c* in the reaction with C*c*O from 6.3 to 4.5 μM. Similar to Tyr[48] and Tyr[97] phosphorylation, Thr[28] phosphorylation leads to partial inhibition of respiration, which we propose prevents $\Delta\Psi_m$ hyperpolarization and thus ROS production under non-stressed conditions and have therefore called "controlled respiration."

For a posttranslational modification to be biologically relevant, a significant fraction of the protein should carry the modification. Using high resolution gel electrophoresis, which separates phosphorylated and unphosphorylated Cyt*c*, we found that >80% of the Cyt*c* pool was phosphorylated (Fig. 1*D*, *lane 1*, *top band*).

Overexpression and Purification of Functional and Correctly Folded Cytochrome c Variants in Escherichia coli Cells—We and others have previously shown for tyrosine-phosphorylated Cyt*c* that phosphomimetic replacement of the phosphorylatable residue with the negatively charged glutamate produces functional effects similar to those seen with the *in vivo* phosphorylated protein (10, 13). We thus generated the following Cyt*c* variants based on the mouse sequence and overexpressed them in *E. coli* BL21 (DE3) cells: WT, phosphomimetic T28E, and T28A Cyt*c* as an additional control that cannot be phosphorylated. The purity of Cyt*c* was confirmed by Coomassie staining (Fig. 2*A*) and spectrophotometric analysis, with 410 nm/280 nm ratios >4 (10). All three proteins were fully reducible and correctly folded, as shown by absorption spectra measurements (supplemental Fig. 1*B*) and circular dichroism (supplemental Fig. 1*C*). Similar to our previous study (10), none of the bacterially overexpressed proteins were Ser-, Thr-, or Tyr-phosphorylated (not shown). The redox midpoint potential of Cyt*c* is approximately midway between the redox potentials of complexes III and IV, and values reported in the literature range from 220 to 270 mV (14). The redox potentials for WT, T28A, and T28E were 246, 221, and 217 mV (Fig. 2*B*), suggesting that a modification on position 28 lowers the redox potential of Cyt*c*, similarly to phosphomimetic Y48E Cyt*c* (10).

Phosphomimetic Cytc Displays a Significantly Decreased Reaction Rate with Isolated CcO—We showed that *in vivo* phosphorylated Cyt*c* displayed an ~50% inhibition in the reaction with isolated bovine liver C*c*O (Fig. 1*C*). To demonstrate that T28E is a good model for Thr[28]-phosphorylated Cyt*c*, we first analyzed its activity in the reaction with purified C*c*O. As shown in Fig. 2*C*, we found that respiration rates of phosphomimetic T28E and T28A Cyt*c* were 73 and 51% reduced, respectively, indicating that T28E Cyt*c* serves as a useful model. The apparent K_m of Cyt*c* in the reaction with C*c*O was 7.8, 9.3, and 4.7 μM for unphosphorylated WT, T28E, and T28A Cyt*c*, respectively. The fact that the inhibitory effect of the phosphomimetic substitution is even more pronounced than that observed with *in vivo* phosphorylated Cyt*c* may be due to the subfraction (about 20%) of unphosphorylated Cyt*c* present when isolated from kidneys. The finding that T28A Cyt*c* also differs from the WT suggests an unexpected structural sensitivity of the reaction to the precise residue at position 28 in Cyt*c* (see "Discussion").

T28E Cytc Can Trigger Caspase-3 Activation but Shows Distinct Features in its ROS-related Functions—To test the possible effect of Thr[28] phosphorylation on apoptotic function, we analyzed the ability of the Cyt*c* variants to trigger apoptosis by measuring downstream activation of caspase-3 using a cell-free caspase assay. Cyt*c* mutants were incubated with cytosolic fractions prepared from mouse lung fibroblasts in which both the somatic and testes-specific isoforms of Cyt*c* were knocked out (15). The T28E mutant was able to activate caspase-3 similarly to wild-type Cyt*c* protein (Fig. 2*D*) and Thr[28]-phosphorylated Cyt*c* (supplemental Fig. 2), indicating that Thr[28] phosphorylation of Cyt*c* does not affect the function of Cyt*c* at the level of apoptosome formation. Other functions of Cyt*c* include ROS scavenging, such as reduction by superoxide to regenerate oxygen or oxidation by H_2O_2. We therefore tested the ability of Cyt*c* in the reaction with H_2O_2 and with the reductant ascorbate. To analyze the former, ferro-(Fe^{2+})-Cyt*c* variants were oxidized in the presence of 100 μM H_2O_2. The T28E phosphomimetic mutant was oxidized at a rate similar to WT Cyt*c*, whereas the T28A mutant was oxidized at a 2.7-fold higher rate (Fig. 2*E*). At higher ROS load, Cyt*c* can lose its functionality through oxidative modifications, which can be monitored through a decrease in the absorption of the heme Soret band at 408 nm present in intact Cyt*c*. After the addition of excess H_2O_2 (3 mM) T28E Cyt*c* was more resistant to degradation by excess H_2O_2 than the wild type, whereas the T28A mutant was degraded more rapidly (Fig. 2*F*), suggesting that the introduction of a negative charge in position 28 stabilizes the protein. To determine the rate of Cyt*c* reduction, ferri-(Fe^{3+})-Cyt*c* variants were reduced in the presence of 200 μM ascorbate. T28E Cyt*c* was reduced at about twice the rate of WT or T28A Cyt*c* (Fig. 2*G*), suggesting that it can act as a superior electron acceptor and scavenger.

Cardiolipin (CL) oxidation is a pro-apoptotic function of Cyt*c*. Native Cyt*c* has a low degree of peroxidase activity, which increases when CL binds to Cyt*c*, causing partial unfolding (16). To assess the peroxidase activity of Cyt*c*, the rate of Amplex Red oxidation by CL-peroxide was analyzed in the presence of H_2O_2. H_2O_2 is a poor substrate for Amplex Red oxidation, whereas oxidized CL species are good substrates. At higher tetralinoleyl-CL (TOCL)/Cyt*c* ratios, T28E Cyt*c* showed significantly reduced peroxidase activity compared with WT (Fig. 2*H*). Interestingly, the T28A mutant had the highest peroxidase activity at all ratios, suggesting that it unfolds more easily compared with WT and T28E Cyt*c*.

High Resolution X-ray Crystallography and Molecular Dynamics Reveal Structural Features of the Thr[28] Epitope—To gain a better understanding of the structure-function relationship of the Thr[28] epitope, we crystalized all three mouse Cyt*c* variants under oxidizing conditions and obtained crystals that diffracted at a resolution of 1.12, 1.36, and 1.30 Å for WT, T28A, and T28E Cyt*c*, respectively. The WT structure has the highest

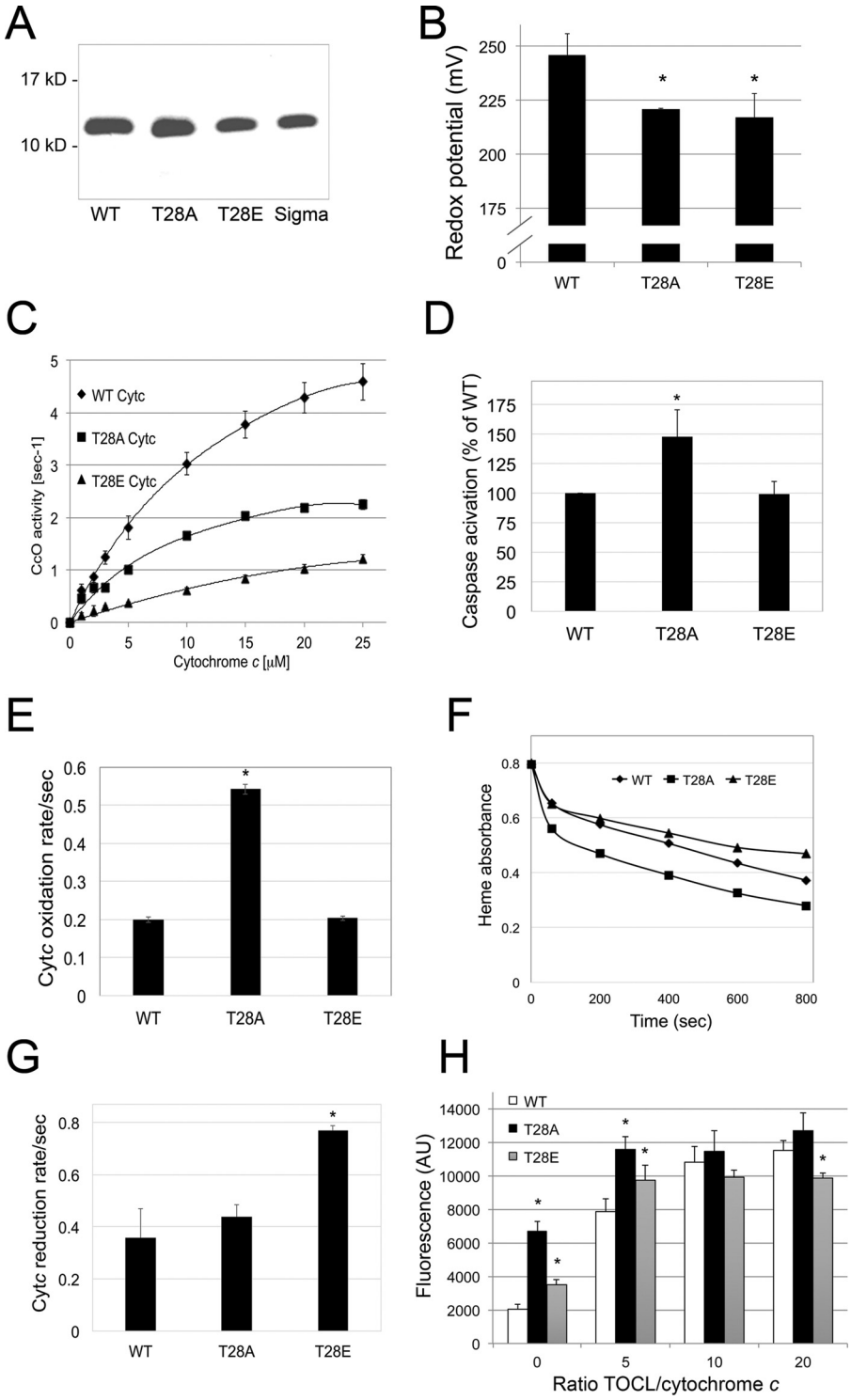

FIGURE 2. **Phosphomimetic T28E Cytc shows unique features *in vitro*.** *A*, Coomassie gel of bacterially overexpressed and isolated WT, T28E (T28E), and T28A (T28A) Cyt*c* indicates that the proteins were purified to homogeneity (Sigma; commercially available bovine Cyt*c* as an additional control). *B*, redox potential is reduced in the T28E and T28A mutants compared with WT; means ± S.D. (*error bars*) are reported; *, $p < 0.05$. *C*, O_2 consumption rates of cow cytochrome *c* oxidase in the reaction with Cyt*c* were 73 and 51% reduced for T28E and T28A Cyt*c* compared with WT. *D*, *in vitro* caspase-3 activity is unaltered with T28E Cyt*c*, whereas it is increased with the T28A mutant. *E*, oxidation rate of WT and T28E Cyt*c* in the presence of H_2O_2 is similar, whereas the T28A mutant shows increased rates. *F*, compared with WT, loss of the heme group by excess H_2O_2 is decreased and increased for T28E and T28A Cyt*c*, respectively. Shown are representative heme destruction curves. *G*, the T28E Cyt*c* reduction rate in the presence of ascorbate is increased compared with WT and T28A Cyt*c*. *H*, T28E Cyt*c*-mediated cardiolipin oxidation is decreased at highest TOCL/Cyt*c* ratios compared with WT and T28A Cyt*c*. *AU*, arbitrary units.

resolution of any mammalian Cyt*c* structure. As expected, the crystal structures of WT, T28A, and T28E are similar overall (Fig. 3, *A*, *D*, and *G*, and supplemental Table 1). To explore possible differences in their solution structures, molecular dynamics simulations were performed on the A chain from the three protein structures as well as on a model of phosphorylated

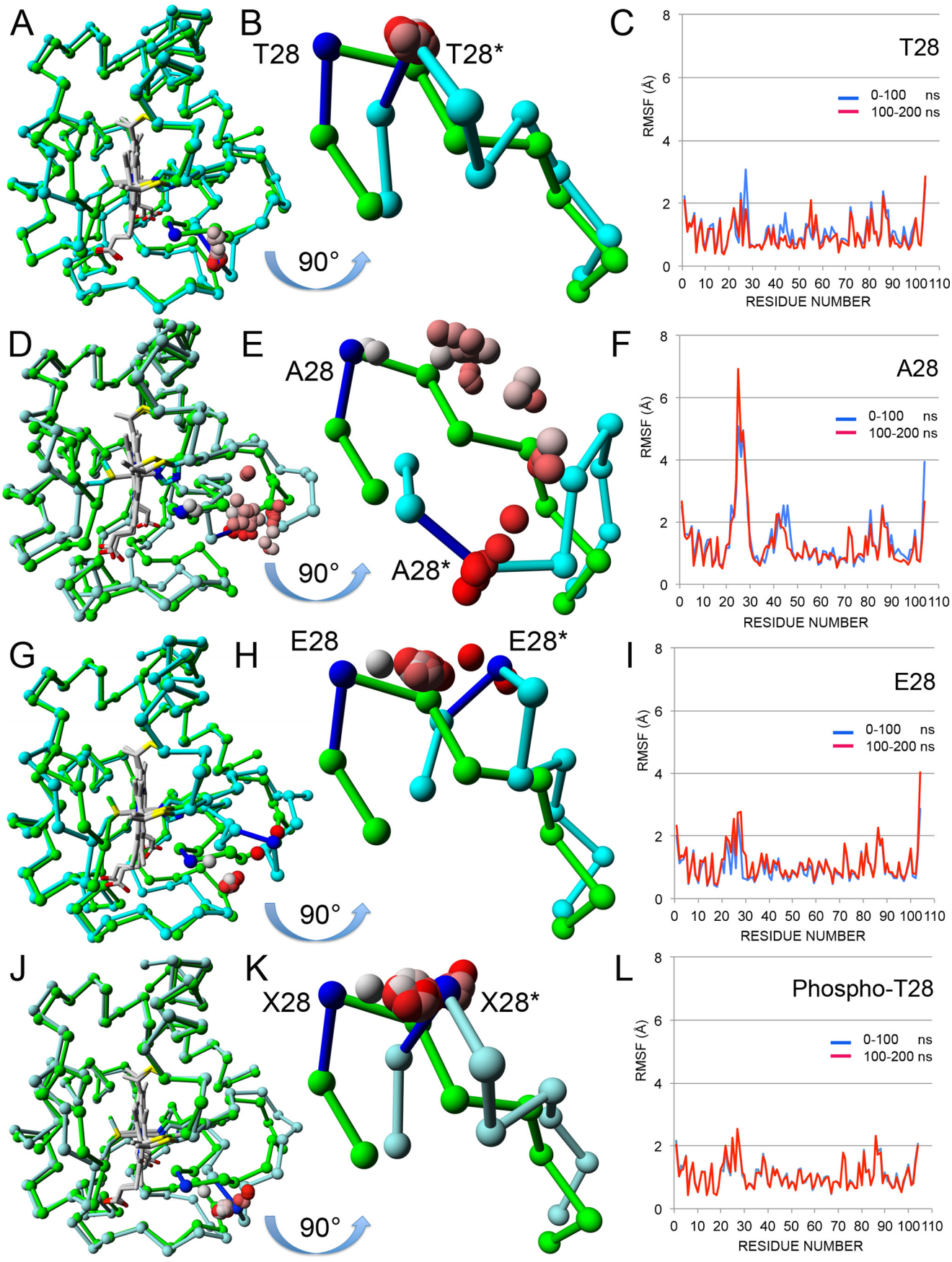
A
B
T28
T28*
90°
C
T28
RMSF (Å)
0-100 ns
100-200 ns
RESIDUE NUMBER
D
E
A28
A28*
90°
F
A28
RMSF (Å)
0-100 ns
100-200 ns
RESIDUE NUMBER
G
H
E28
E28*
90°
I
E28
RMSF (Å)
0-100 ns
100-200 ns
RESIDUE NUMBER
J
K
X28
X28*
90°
L
Phospho-T28
RMSF (Å)
0-100 ns
100-200 ns
RESIDUE NUMBER

Cyt*c* with the phosphate group added to Thr[28] in the WT chain A using COOT (PDB code Tpo[28]). In all four simulations, the Cα chain from the final solution structure after 200 ns superposed well with the beginning crystal structure except for the Thr[28]-containing loop 22–30 (Fig. 3, *A*, *B*, *D*, *E*, *G*, *H*, *J*, and *K*), which also had the highest root mean square fluctuations (RMSF) except for the N and C termini (Fig. 3, *C*, *F*, *I*, and *L*). In all four simulations, the surface loop adopted an alternate conformation, which moved the Cα atom of residue 28 about 5 Å from its starting position. Surprisingly, in the T28A simulation, the loop paused at the same conformation as the others but then continued to move until it reached a conformation after 200 ns that put Ala[28] 11.9 Å from its starting position (Fig. 3*E*). These differences may explain the structural instability of this mutant. In contrast, T28E Cyt*c* recapitulates the functional effects seen with *in vivo* phosphorylated Cyt*c*. As expected, electrostatic potential (ESP) calculations show that the T28E mutant has a negative ESP region that is larger than WT and is only exceeded by the Thr[28] → Thr(P) model (supplemental Fig. 4, *B–D*).

Introduction of T28E Cytc into Cytc Double Knock-out Cells Reduces Oxygen Consumption Rate, Mitochondrial Membrane Potential, and ROS—To test the effect of phosphomimetic substitution of Cyt*c* in intact cells on mitochondrial parameters, we generated cell lines stably transfected with empty vector control and WT, T28E, and T28A Cyt*c*, using mouse lung fibroblasts in which both the somatic and testes-specific Cyt*c* isoforms have been knocked out. Double knock-out is required because cultured mouse cells lacking somatic Cyt*c* induce the expression of the testes isoform, restoring mitochondrial respiration (15). Expression levels of WT and T28E Cyt*c* were comparable between different clones, whereas protein levels of T28A Cyt*c* were lower compared with the other Cyt*c* variants (the clone with the highest expression levels was used for subsequent experiments; Fig. 4*A*), suggesting that higher expression levels of this mutant may interfere with cellular functions or that protein turnover is higher. As reported previously (17), Cyt*c* knock-out interferes with complex I and IV assembly, which is restored upon reintroduction of the three Cyt*c* variants (Fig. 4*A*). Determination of cell growth showed that WT and T28E Cyt*c*-expressing cells grew equally well, whereas T28A Cyt*c*-expressing cells showed a 27% reduced growth rate *versus* WT (Fig. 4*B*) (see "Discussion"). We next analyzed intact cell respiration. Strikingly, cells expressing T28E phosphomimetic Cyt*c* showed 60% reduced respiration rates (Fig. 4*C*), matching results obtained with purified C*c*O *in vitro* (Figs. 1*C* and 2*C*). This finding is of importance because it suggests that a modification of the small electron carrier Cyt*c* can control overall flux in the ETC, a scenario that has not been reported or considered in the past. Consequently, a reduction of the respiration rate should translate into a reduced mitochondrial membrane potential $\Delta\Psi_m$. Analysis with the voltage-dependent probe JC-1 showed that T28A- and T28E-expressing cells showed 15 and 31% reduced fluorescence compared with WT (Fig. 4*D*), indeed indicating a reduction of $\Delta\Psi_m$. Given the direct connection of $\Delta\Psi_m$ with ROS production at complexes I and III (18), we predicted that T28E Cyt*c*-expressing cells should exhibit reduced ROS levels. Using the mitochondrial ROS probe MitoSox, we found that fluorescent signals were reduced by 35–40% in cells expressing T28E and T28A Cyt*c* compared with WT, indicating reduced ROS levels (Fig. 4*E*). ATP levels were reduced by 6 and 28% for cells expressing T28A and T28E, respectively (Fig. 4*F*). To test whether cells expressing T28E Cyt*c* are better protected from H_2O_2 exposure, cell viability was determined after treatment with H_2O_2. T28E Cyt*c*-expressing cells showed higher viability when treated with a low concentration of H_2O_2, but viability matched with WT Cyt*c*-expressing cells at higher H_2O_2 concentration (Fig. 4*G*). This observation suggests that T28E Cyt*c* protects the cells from mild oxidative stress. These data suggest that modification of Cyt*c* Thr[28] regulates ETC flux, which in turn affects $\Delta\Psi_m$ and ROS.

AMPK Interacts with and Phosphorylates Cytc on Thr[28]—To identify a kinase candidate that targets Cyt*c* for Thr[28] phosphorylation, we first used the online tool Scansite (19) for *in silico* prediction of possible Cyt*c* binding motifs of signaling molecules. Interestingly, Thr[28] was predicted to be an AMPK phosphorylation site. The epitope has several features identified in known AMPK targets, including a lysine in positions −6 and −3 and a proline and a leucine residue in positions +2 and +4, respectively (20).

In comparison with other tissues, AMPK in the kidney shows distinctive features and has a high activity already under basal conditions (see "Discussion"), making it a good candidate for Cyt*c* phosphorylation because we purified it directly from kid-

FIGURE 3. **Structural and molecular dynamics analyses.** *A*, chain A from the WT crystal structure (PDB entry 5C0Z) before (*green*) and after (*cyan*) 200 ns of molecular dynamics are shown as Cα tracings superimposed using only main chain atoms. The hemes (Hec201) are shown in *gray*. The average Thr[28] Cα positions for the 39 intermediate 5-ns steps between the two end points are shown as *spheres colored* in a *gradient* from *gray* (5 ns) to *red* (195 ns). *B*, the mobile loop (amino acids 22–30) from *A* is shown in greater detail after rotation by 90° about its horizontal axis to generate a "bottom-up" view. The Cα atoms for the starting (Thr[28]) and ending (Thr[28]*) structures are *colored blue*. The intermediate Cα atoms (*gray* to *red*) all cluster about Thr[28]*, showing that the loop jumps immediately to its minimum energy position and stays there. The distance between Thr[28] Cα and Thr[28]* Cα is 4.5 Å. *C*, the RMSF for the first 100 ns (*blue line*) and the second 100 ns (*red line*) by residue are plotted together. Two RMSF values (Lys[27] and Ala[44]) are noticeably lower in the second 100 ns. *D*, chain A from the T28A crystal structure (PDB entry 5C9M) before (*green*) and after (*cyan*) 200 ns of molecular dynamics. See *A* for details. *E*, equivalent to *B*, except the two loops are from *D*. Over the 200 ns, the Cα atom of Ala[28] pauses at four distinct intermediate positions before clustering around the final position. The distance between Ala[28] Cα and Ala[28]* Cα is 11.9 Å. *F*, equivalent to *C* for T28A Cyt*c*. The RMSF values for Ala[44] are lower in the second 100 ns, but those for Lys[27] are significantly higher in the second 100 ns, in fact the highest seen in all four RMSF plots. *G*, chain A from the T28E crystal structure (PDB entry 5DF5) before (*green*) and after (*cyan*) 200 ns of molecular dynamics. See *A* for details. *H*, equivalent to *B*, except the two loops are from *G*. Over the 200 ns, the Cα atom of Glu[28] clusters at a midway position before moving to its final position near the end of the simulation. The distance between Glu[28] Cα and Glu[28]* Cα is 7.2 Å. *I*, equivalent to *C* for T28E Cyt*c*. The RMSF values for Ala[44] are of average size and similar for both halves of the simulation. The RMSF values for the loop containing Glu[28] are higher than average but similar for both halves of the simulation. *J*, the Cα tracings of chain A from the WT crystal structure (PDB entry 5C0Z) with a phosphate group modeled onto Thr[28] are shown superposed before (*green*) and after (*cyan*) 200 ns of molecular dynamics. See *A* for details. *K*, equivalent to *B*, except the two loops are from *J*. Over the 200-ns period, the Cα atom of Thr(P)[28] moves quickly to the final position and clusters around it. The distance between Xaa[28] (*X28*) Cα and Xaa[28]* Cα is 5.2 Å. *L*, equivalent to *C* for the Tpo[28] model. The RMSF values for the loop containing Glu[28] are higher than average but similar for both halves of the simulation.

ney without manipulation of signaling pathways. To test whether AMPK can phosphorylate Cyt*c*, we first performed an *in vitro* kinase assay with commercially available AMPK and unphosphorylated WT Cyt*c* as substrate. As shown in Fig. 5*A*, Cyt*c* was phosphorylated in a specific and AMPK-dependent manner, which could be further accelerated by the addition of AMPK activator AMP (Fig. 5*B*). We next confirmed by mass spectrometry that Thr[28] was the site of *in vitro* AMPK phos-

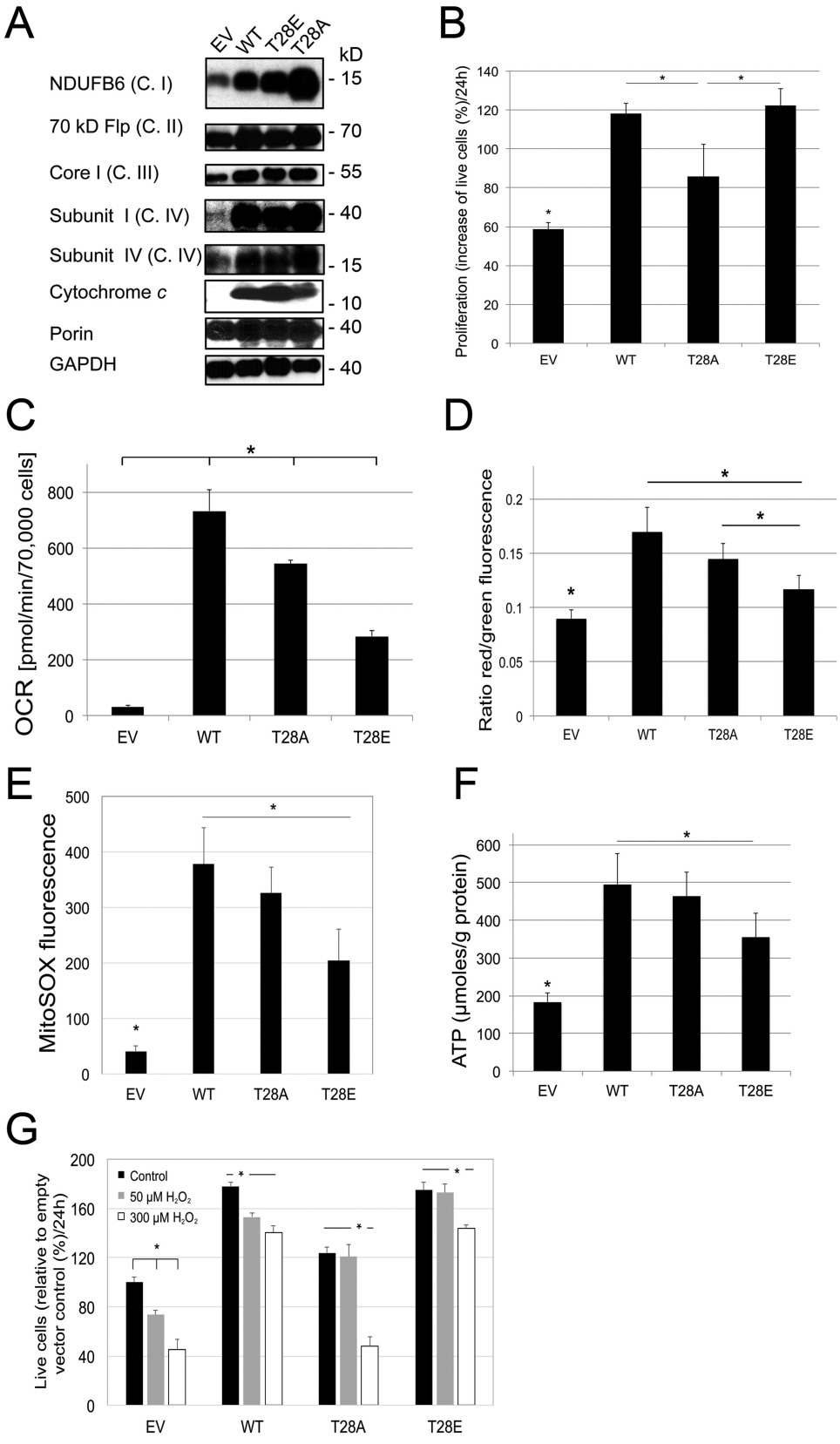

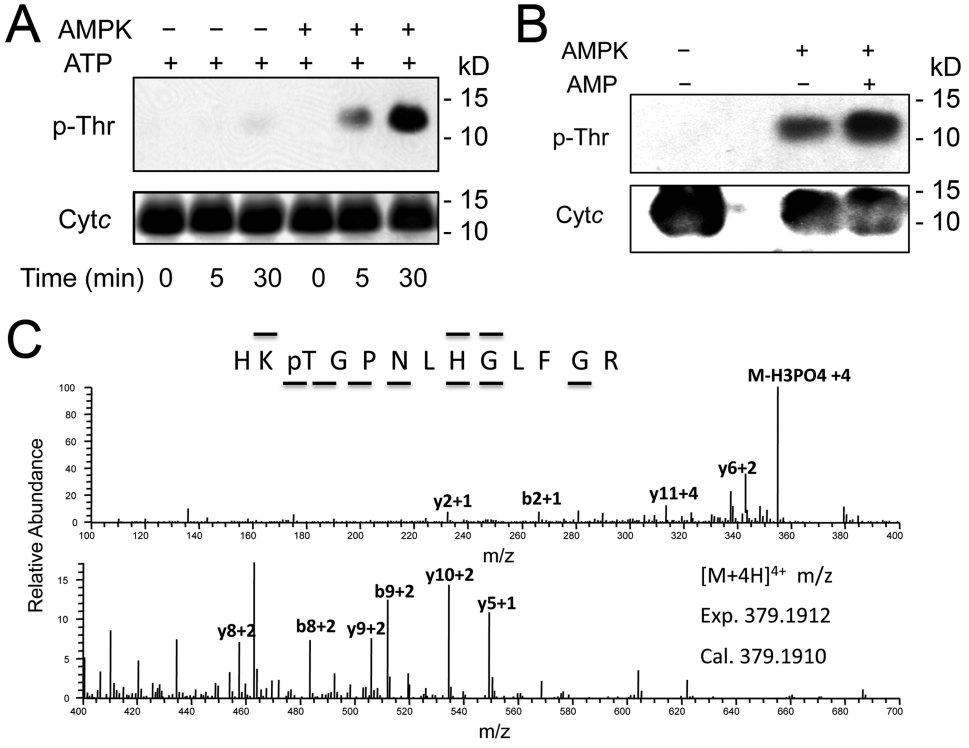

FIGURE 5. **AMPK phosphorylates Cyt*c* on Thr[28] *in vitro*.** *A*, *in vitro* AMPK kinase assay with cow heart Cyt*c*, conducted in the absence of AMPK activator AMP, shows a time-dependent increase of threonine phosphorylation, as determined by Western blotting analysis. *B*, *in vitro* AMPK kinase assay with cow heart Cyt*c* shows an increase of threonine phosphorylation in the presence of AMPK activator AMP. *C*, Cyt*c* subjected to an *in vitro* AMPK kinase assay as in *A* is phosphorylated on Thr[28] as determined by the nano-LC/ESI/MS/MS spectrum of HKpTGPNLHGLFGR. The phosphorylation site was unambiguously assigned by fragment ions y10 and y11. The sequence of the peptide was assigned by b2, b8, b9, y2, y5, y6, y8, y9, and y10.

phorylation (Fig. 5*C*). For AMPK to phosphorylate Cyt*c* in kidney, the proteins have to physically interact inside the cell. Under basal conditions, co-immunoprecipitation experiments using extracts from total mouse kidney tissue as well as highly purified mitochondria show interaction of AMPK with Cyt*c* (Fig. 6*A*). Furthermore, submitochondrial fractionation of highly purified mitochondria indicates that AMPK and its activated phosphorylated form are present in the mitochondrial intermembrane space (Fig. 6*B*, *lane 2*), as is Cyt*c*. Finally, activation and inhibition of AMPK in mouse kidney tissue using A769662 and Compound C, as confirmed by phosphorylation of AMPK target phosphoacetyl-CoA carboxylase (Fig. 6*C*), results in increased and decreased threonine phosphorylation of Cyt*c*, respectively (Fig. 6*D*), which inversely correlates with intact mitochondrial respiration rates (Fig. 6*E*), mirroring data presented in Figs. 1, 2, and 4. It is important to note that no such effects were observed using liver tissue (data not shown), suggesting tissue-specific differences in the regulation of Cyt*c*, which agrees with our previous studies demonstrating that liver Cyt*c* is Tyr[48]-phosphorylated.

Discussion

Little is known about the regulation of mitochondrial oxidative phosphorylation by cell signaling. We have previously reported two distinct tyrosine phosphorylation sites on Cyt*c* from mammalian heart and liver tissue. The current report functionally characterizes a third tissue-specific phosphorylation site, Thr[28], on Cyt*c* purified from kidney. The same site was also mapped, but not further studied, in a high throughput mass spectrometry study using resting human skeletal muscle (21), suggesting that Thr[28] can be targeted to regulate ETC function beyond kidney tissue. For the Cyt*c* we isolated from kidney, the majority (between ~60 and 80%, depending on the preparation) of the protein is phosphorylated at Thr[28]. In addition, we mutated Thr[28] to phosphomimetic glutamate and non-phosphorylatable alanine to further characterize the effects of this phosphorylation *in vitro* and in cultured murine lung fibroblast cells lacking both Cyt*c* isoforms.

Bovine *in vivo* phosphorylated and unphosphorylated Cyt*c* as well as overexpressed mouse WT, T28E, and T28A Cyt*c* generated hyperbolic kinetics in the reaction with purified bovine

FIGURE 4. **Introduction of phosphomimetic Cyt*c* into Cyt*c* knock-out cells leads to controlled respiration, intermediate mitochondrial membrane potentials, and low ROS levels.** *A*, Western blotting of Cyt*c* double knock-out lung fibroblasts stably transfected with empty vector (*EV*) and WT, T28A, and T28E expression constructs. *B*, proliferation rates of stably transfected lines were determined by cell counts; means ± S.D. (*error bars*) are reported; *, $p < 0.05$. *C*, intact cell oxygen consumption rates (*OCR*) are decreased in both Cyt*c* mutants. *D*, mitochondrial membrane potential as determined by JC-1 fluorescence was decreased in cells expressing T28E *versus* WT and T28A Cyt*c*. *E*, basal mitochondrial reactive oxygen species generation as determined with MitoSOX is decreased in cells expressing T28E Cyt*c* compared with WT. *F*, ATP levels determined with the bioluminescent method were decreased in cells expressing T28E Cyt*c* compared with WT. *G*, live cell counts after treatment with H_2O_2 indicate that T28E-expressing cells are better protected at intermediate H_2O_2 levels compared with WT, whereas T28A-expressing cells show decreased survival at all concentrations compared with WT. *Error bars*, S.D.

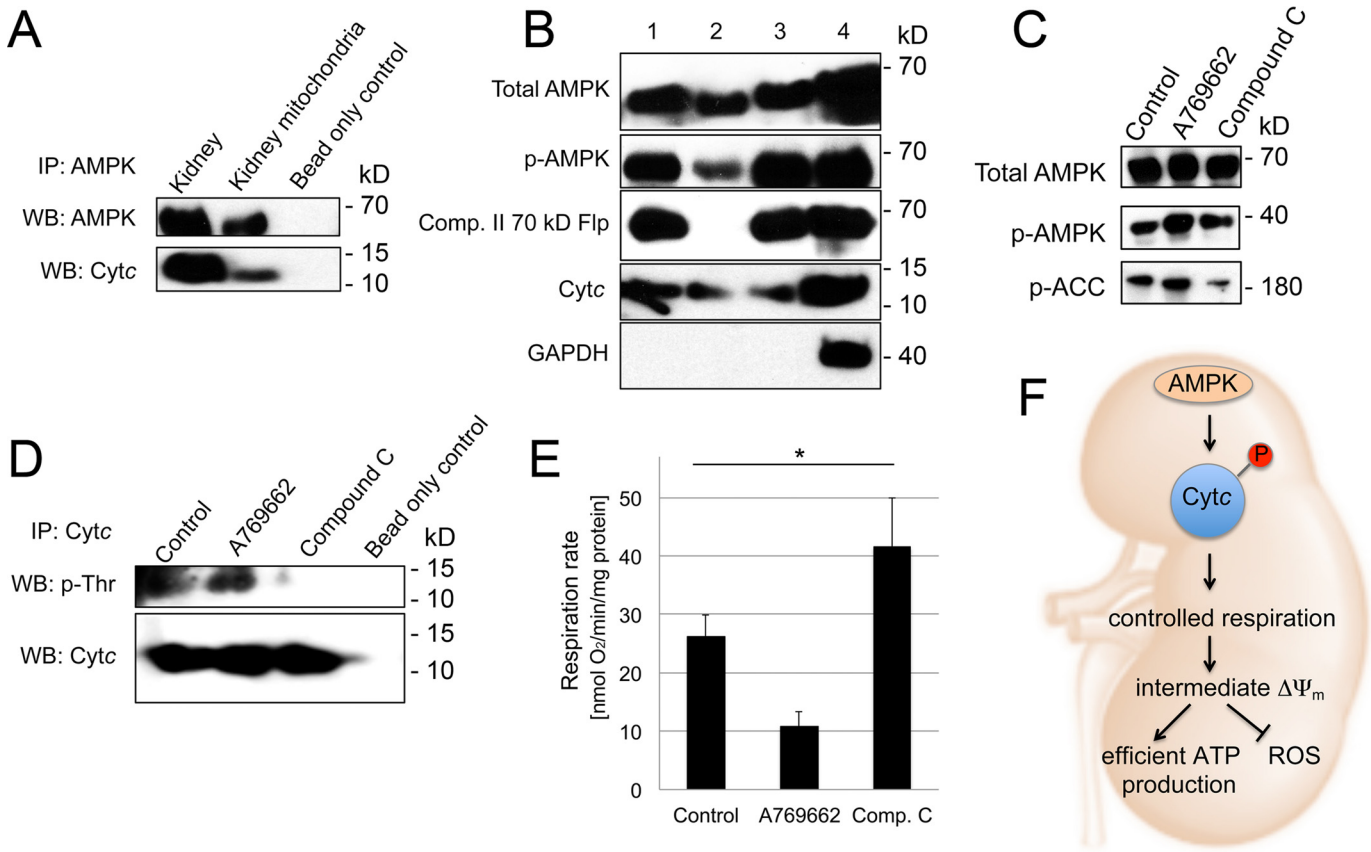

FIGURE 6. **AMPK interacts with Cytc and localizes to the mitochondria.** *A*, immunoprecipitation (*IP*) of AMPK from total mouse kidney extracts shows interaction of AMPK with Cytc. *B*, submitochondrial fractionation of sucrose gradient purified mouse kidney mitochondria shows AMPK and phospho-AMPK localization to the mitochondrial intermembrane space (*IMS*). *Lane 1*, mitochondrial lysate; *lane 2*, intermembrane space; *lane 3*, pellet after outer mitochondrial membrane permeabilization containing outer mitochondrial membrane, mitoplasts, and residual IMS; *lane 4*, kidney tissue homogenate. *C*, incubation of mouse kidney tissue with AMPK activator A769662 and inhibitor Compound C leads to activation and inhibition of AMPK, respectively, as deduced by AMPK target phosphoacetyl-CoA carboxylase (*p-ACC*). *D*, pull-down of Cytc from mouse kidney tissue after treatment with AMPK activator A769662 and inhibitor Compound C leads to an increase and decrease of Cytc threonine phosphorylation, respectively. *E*, incubation of mouse kidney tissue with AMPK activator A769662 and inhibitor Compound C leads to decreased and increased intact mitochondrial respiration, as determined in tissue homogenates; means ± S.D. (*error bars*) are reported; *, $p < 0.05$. *F*, model of the regulation of electron transport chain activity through phosphorylation of Cytc. Under healthy conditions, Cytc is phosphorylated, leading to a partial inhibition of mitochondrial respiration. This in turn maintains healthy intermediate $\Delta\Psi_m$ values that are sufficient for effective energy production but prevent the generation of ROS, which occurs at pathologically high $\Delta\Psi_m$ values.

liver C*c*O. Compared with WT, maximal turnover was reduced by 50 and 73% for *in vivo* phosphorylated and phosphomimetic Cyt*c*, respectively. Furthermore, expression of phosphomimetic T28E Cyt*c* led to a reduction of respiration in intact cells, suggesting for the first time that modification of the small electron carrier can control overall ETC flux. These findings are consistent with the concept that phosphorylation of mitochondrial proteins, in general, down-regulates whereas dephosphorylation activates mitochondrial function (22). Reduced respiration rates both *in vitro* with purified C*c*O and in intact cells expressing T28E Cyt*c* may be a result of the observed change in the redox midpoint potential as well as of structural changes in the protein. Thr[28] lies in the center of an unusual structural element termed the "negative classical γ turn," which is composed of residues 27–29 and is important for the stability of Cyt*c* (23). Thr[28] is a surface residue close to the solvent exposed and accessible tip of the heme group that mediates electron transfer to C*c*O. It is located on the frontal right side of the molecule in the conventional view (Fig. 3*A*), which is part of the circular, positively charged epitope surrounding the heme crevice with which Cyt*c* binds to the corresponding negatively charged epitope on C*c*O (24). Interestingly, in this computational Cyt*c*-C*c*O docking model, Thr[28] is located at the interface of catalytic subunits I and II and nuclear encoded subunit VIIc, with closest distances of <6 Å to Lys[47] of subunit VIIc and of <7 Å to Asp[50] of subunit I and Trp[104] and Ser[202] of subunit II (supplemental Fig. 4*G*). Two of the four C*c*O residues are particularly noteworthy. Asp[50] is one of only a handful of residues in the entire C*c*O complex that have noticeably different geometries between the reduced and oxidized state in the crystal structure (25). In addition, Asp[50] is located next to another flexible amino acid, Asp[51], which, when mutated to Asn, blocks proton pumping of the enzyme and was proposed to be the proton ejection site of C*c*O (26). Phosphorylation of Thr[28] may interfere with the outward movement of the Asp[50]-Asp[51] region and thus the opening of the proposed proton exit channel during reduction of C*c*O. This would lead to inhibition of C*c*O by inhibiting electron transfer-coupled proton pumping. Alternatively, repulsion between phospho-Thr[28] and Asp[50] may result in suboptimal binding to C*c*O, causing reduced respiration rates. The second interesting interaction site on C*c*O is Trp[104], which is the site on C*c*O where electrons from Cyt*c*

enter before reaching the first metal center, the binuclear Cu_A site. Spatial interference upon Cyt*c* Thr[28] phosphorylation with Trp[104], which is essential for catalysis, could also explain reduced activity.

We have previously shown that phosphomimetic Y48E Cyt*c* is incapable of downstream caspase activation (10). In contrast, phosphorylation of Cyt*c* Thr[28] or its phosphomimetic substitution does not interfere with the ability of Cyt*c* to trigger downstream caspase activation. This difference agrees with the observation that the Tyr[48] epitope is directly involved in the interaction of Cyt*c* with Apaf-1 whereas the Thr[28] epitope is not (27). This ability to similarly inhibit CcO activity but differently affect caspase activation is an example of tissue-specific signaling, which in this case may result from AMPK isoform expression in a tissue-specific manner.

A recent study compared 285 Cyt*c* sequences across all phyla from humans to bacteria (28). Overall, threonine is the most common amino acid at position 28 and is conserved in mammals. However, in some non-mammalian organisms, five other amino acids can also be found, namely Gln, Val, Ile, Ser, and even the phosphomimetic Glu, which is present in several plants, including potatoes and tomatoes. Interestingly, alanine is not among the residues evolutionarily tolerated in this position. Another study using T28A mutant Cyt*c* also reported decreased respiration rates with C*c*O (29), confirming our results. We found that T28A Cyt*c* has a higher ability to activate downstream caspases and unfolds more easily, which increases CL oxidation. Its instability compared with WT and T28E Cyt*c* is also suggested in the respective circular dichroism spectra (supplemental Fig. 1*C*, see lower wavelength range). In addition, T28A Cyt*c* is most rapidly oxidized and degraded in the presence of H_2O_2. Structural analysis of all three Cyt*c* variants shows that the amino acids comprising the negative classical γ turn element display by far the highest root mean square deviation values compared with any other Cyt*c* sequence, suggesting that the Thr[28] epitope is the most flexible element of the entire molecule. A plot of the average temperature factors, which for these high resolution structures are a reasonable measure of local mobility, also showed, other than at the termini, that the highest relative values occurred at the 22–30 loop for all three structures. Furthermore, molecular dynamics simulations of crystalized T28A Cyt*c* produce a structure in which the Thr[28] Cα atom is moved by 11.9 Å, approximately twice as far compared with WT, T28E, and modeled phospho-Thr[28] Cyt*c* (Fig. 3). These findings collectively suggest that alanine was evolutionarily selected against because it introduces additional flexibility at a site near the heme crevice, probably due to its small size, leading to a detrimental reduction of protein stability and interference with its multiple functions. This may also at least in part account for the finding of lower Cyt*c* protein levels in cells expressing this mutant. Another evolutionarily forbidden substitution, T28D, which introduces a negative charge, also generates "rogue" functional changes in Cyt*c*, as seen in the reaction with C*c*O, that are even opposite (29) of what we report for *in vivo* phosphorylated Cyt*c*, whereas glutamate replacement, as used here, produces the same functional effects as phosphorylated Cyt*c*.

Our studies suggest that AMPK targets Cyt*c* for Thr[28] phosphorylation within the mitochondria. Future work using a genetic approach should be conducted to confirm the role of AMPK in Cyt*c* phosphorylation. However, because kidneys express both the AMPK-α1 and -α2 catalytic isoforms and because their double knock-out results in embryonic lethality (30), a more advanced approach would be necessary, such as a tissue-specific knock-out.

AMPK is one of the most important and evolutionarily oldest metabolic sensors and regulators (31). It is implicated in human disease, including diabetes, where its activity is impaired in several organs, including the kidneys (32). Generally, AMPK promotes catabolic processes, and it is activated by phosphorylation and allosterically under conditions when ATP levels drop and AMP levels increase. However, our understanding of the role of AMPK specifically in the kidney is in its infancy (33), and there are reports suggesting that it operates differently in this organ compared with other tissues. For example, AMPK is already active in the kidney under basal conditions and shows a paradoxical decrease in activity in a rat kidney ablation and infarction model (34), a condition when energy depletion and thus demand is maximal. In cells from patients with hereditary leiomyomatosis renal cell cancer, the Krebs cycle is inhibited, which also leads to a paradoxical decrease of AMPK activity (35). The high basal activity of AMPK also observed in this study (Fig. 6, *B* and *C*) may be due to the fact that kidneys are always active and rely heavily on oxidative phosphorylation (12). Consistent with our findings that AMPK-mediated Cyt*c* phosphorylation partially suppresses mitochondrial respiration, it was shown in human renal proximal tubular epithelial cells that additional activation of AMPK with metformin results in a significant reduction of cellular respiration (36).

The strong periodicity of kidney function (37, 38) (*i.e.* activity oscillations controlled by circadian rhythm) provides a potential rationale for the buffering against rapid increase in ETC activity, with attendant ROS increase, provided by the paradoxical AMPK response found in kidney. We thus propose a model, shown in Fig. 6*F*, in which under physiological conditions a central role of Cyt*c* Thr[28] phosphorylation in kidney is to maintain optimal intermediate $\Delta\Psi_m$ levels, which allow efficient energy production but prevent ROS generation because ROS are produced at high $\Delta\Psi_m$ levels (reviewed in Ref. 39). In line with our concept, it was shown in cultured mouse proximal tubular cells subjected to various forms of metabolic stress that genetic or pharmacologic inhibition of AMPK caused apoptosis. Furthermore, in rats subjected to renal ischemia/reperfusion injury, application of a high dose of AMPK activator AICAR shortly before ischemia significantly improves cell survival (40). Cyt*c* purified from ischemic kidney is dephosphorylated (not shown), similar to Cyt*c* isolated from ischemic brain (41). This would allow maximal ETC flux, $\Delta\Psi_m$ hyperpolarization, and ROS production during reperfusion when ETC function is reinstated due to reintroduction of oxygen. We have shown that neuroprotective insulin treatment before brain ischemia/reperfusion leads to Cyt*c* Tyr[97] phosphorylation, which also decreases respiration, resulting in suppression of the release of Cyt*c* from the mitochondria and a 50% reduction of neuronal death (41). It will be interesting to see in future studies

whether AICAR treatment maintains Cyt*c* Thr^{28} phosphorylation during ischemia in the kidney, alleviating ETC hyperactivation during reperfusion.

In conclusion, all three functionally studied Cyt*c* phosphorylations to date (Tyr^{97}, Tyr^{48}, and Thr^{28}) lead to a partial inhibition in the reaction with C*c*O, or "controlled respiration" (Fig. 6*F*). We propose that this mechanism provides a basis for the maintenance of "healthy" intermediate $\Delta\Psi_m$ levels under normal conditions. This, in turn, prevents excessive ROS production that occurs at high $\Delta\Psi_m$ levels under conditions of stress when mitochondrial proteins become dephosphorylated, allowing maximal ETC flux, $\Delta\Psi_m$ hyperpolarization, excessive ROS, and cell death. Although all three known Cyt*c* phosphorylations limit respiration, the choice of site in a particular tissue may depend on tissue-specific metabolic differences or on additional effects of the phosphorylation, such as regulation of apoptosis.

Experimental Procedures

Isolation of Cytochrome c from Bovine Kidney Tissue—Reagents and chemicals were purchased from Sigma unless stated otherwise. All procedures involving animal tissues were approved by the Wayne State University institutional animal care and use committee. Kidneys from freshly slaughtered cows were snap-frozen on dry ice and stored at −80 °C until used for Cyt*c* purification by the acid extraction method at 4 °C or on ice (9). Briefly, kidney tissues were homogenized in 100 mM phosphate buffer, pH 4.5, adjusted with acetic acid, and incubated overnight at 4 °C. Under those conditions, most cellular proteins denature and precipitate, whereas Cyt*c* is extracted and stays in solution. The homogenate was centrifuged at 15,810 × *g* for 35 min, supernatants were decanted through cheesecloth, and pH was adjusted to 7.4 with KOH while simultaneously adding protease (1 mM PMSF) and phosphatase inhibitors (10 mM KF, 1 mM sodium orthovanadate), thus preserving the phosphorylation state of Cyt*c*. The supernatant was incubated at 4 °C for 20 min and centrifuged following ion exchange chromatography. First, the supernatant was passed through a DE52 anion exchange column equilibrated with 20 mM phosphate buffer, pH 7.4, 3.6 millisiemens/cm conductance. Cyt*c* was collected in the flow-through, which was pH-readjusted to 6.5 and applied to a CM52 cation exchange column equilibrated with 30 mM phosphate buffer, pH 6.5, 5.5 millisiemens/cm conductance. Cyt*c* bound to the CM52 column was oxidized on the column with 2 mM $K_3Fe(CN)_6$ and was eluted by step gradient using 30, 50, 80, 120, and 150 mM phosphate buffers, pH 6.5. To obtain a highly pure fraction of Cyt*c*, the DE52 and CM52 ion exchange chromatography steps were repeated. For further purification, HPLC size exclusion chromatography with a column equilibrated with 150 mM phosphate buffer, pH 6.5, was performed, and a mixture of phosphorylated and nonphosphorylated Cyt*c* was obtained. The protein was concentrated under vacuum, desalted by centrifugation using Amicon Ultra-15 3 kDa centrifugal filter units (Millipore, Billerca, MA), and stored at −80 °C.

Protein Concentration and Purity Determination—Purified Cyt*c* was reduced with 100 mM sodium dithionite, desalted with NAP-5 columns (GE Healthcare), and analyzed on a Jasco V-570 double beam spectrophotometer (2-nm bandwidth). The concentration was determined by differential spectra at 550 nm by subtracting the oxidized form from the reduced and calculated via $\epsilon(\text{reduced} - \text{oxidized})_{550\ nm} = 19.6\ mM^{-1}\ cm^{-1}$. Purity of the protein was confirmed by Coomassie staining after 12% Tris-Tricine SDS-PAGE.

Gel Electrophoresis and Western Blotting—Western blotting analyses were performed to analyze the phosphorylation status of purified Cyt*c*, with a 1:5,000 dilution of primary antibodies: anti-phosphotyrosine (4G10, Millipore, Billerica, MA), anti-phosphoserine (set of four individual monoclonal antibodies, 1C8, 4A3, 4A9, and 16B4; EMD Biosciences, Gibbstown, NJ), and anti-phosphothreonine antibodies (set of three individual monoclonal antibodies, 1E11, 4D11, and 14B3; EMD Biosciences), followed by a 1:10,000 dilution of anti-mouse IgG or IgM horseradish peroxidase-conjugated secondary antibody (GE Healthcare). EGF-stimulated A431 total cell lysate (Upstate, Billerica, MA) was used as a positive control, and ovalbumin was used as a negative control. Note that sets of four and three antibodies were used for phosphoserine and phosphothreonine detection, respectively, because these epitopes are small and adjacent amino acids contribute to the binding of the antibodies; using a mixture of different clones allows detection of phosphorylated serine and threonine residues in a broad amino acid sequence context. Signal detection was performed with an enhanced chemiluminescence method (GE Healthcare). The following antibodies were used at a dilution of 1:1,000: complex I NDUFB6 (MS108, MitoSciences, Eugene, OR); complex II 70-kDa subunit (MS204, MitoSciences); complex III core I (MS303, MitoSciences); complex IV subunit I (MS404, MitoSciences); complex IV subunit IV (sc58348, Santa Cruz Biotechnology, Inc., Dallas, TX); cytochrome *c* (556433, BD Pharmingen, San Jose, CA); porin (MSA03, MitoSciences); and GAPDH (ab9484, Abcam). To separate Thr^{28}-phosphorylated from unphosphorylated Cyt*c*, a 15% acrylamide, 2.6% bisacrylamide gel (Tris-Tricine-SDS-PAGE) was prepared. Cyt*c* (500 ng) was denatured in 2× sample buffer (NuPAGE, NP0007, Invitrogen) with 100 mM DTT and 3% β-mercaptoethanol. Cathode buffer was 100 mM Tris, 100 mM Tricine, 0.1% SDS, and pH 8.25; anode buffer was 200 mM Tris-Cl pH 8.9; and gels were run at a low voltage (80 V) for up to 4 h.

Mass Spectrometry of Purified Cytochrome c to Detect Site-specific Phosphorylation—Phosphorylation site mapping on purified kidney Cyt*c* was performed after tryptic digestion and TiO_2 enrichment of phosphopeptides, following C18 reversed-phase chromatography as described (41). Peptides were injected into the mass spectrometer (LTQ Orbitrap-Velos, Thermo Scientific, Waltham, MA) after electrospray ionization. MS/MS spectra were obtained in positive ion mode, assigned to peptide sequences from the UniProt protein database, searched with the MASCOT algorithm for posttranslational modifications, and manually verified.

Immunoprecipitation and Western Blotting Analyses from Tissue Homogenates—All Western blotting analyses from tissue homogenates were performed using 20 μg of whole tissue homogenates. All immunoprecipitations from tissue homogenates were performed with 1 mg of tissue homogenate overnight at 4 °C. For immunoprecipitations, 50 μl of bead (Immu-

noCruz IP/WB Optima E and F Systems, sc-45042 and sc-45043) and 5 μg of antibody were allowed to conjugate overnight under rotation at 4 °C, centrifuged (22,000 × *g*) for 30 s, and washed twice with 500 μl of PBS.

Mutagenesis, Expression, and Purification of Cytochrome c Variants—Mouse somatic Cyt*c* cDNA was cloned into the pLW01 expression vector (kind gift from Dr. Lucy Waskell, University of Michigan) that also contained the cDNA encoding heme lyase (CYC3), an enzyme necessary for the covalent attachment of the heme group to apo-Cyt*c*. Thr[28] in the wild type Cyt*c* cDNA was mutated to the phosphomimetic glutamate and nonphosphorylatable alanine as an additional control. Forward primers 5′-AAGCATAAGGAGGGACCAAA-3′ (T_m = 53.8 °C) and 5′-AAGCATAAGGCTGGACCAAA-3′ (T_m = 53.8 °C) and corresponding reverse and complement primers 5′-TTTGGTCCCTCCTTATGCTT-3′ (T_m = 54.6 °C) and 5′-TTTGGTCCAGCCTTATGCTT-3′ (T_m = 54.6 °C) were used for T28E and T28A mutagenesis PCR, respectively, as described (10). The outer primers that amplified the entire Cyt*c* cDNA sequence containing NcoI and BamHI restriction sites were 5′-AATTTACCATGGGTGATGTTGAAAAAG-3′ (T_m = 56.7 °C) and 5′-AATAAAGGATCCAGTGGAATTATTCAT-3′ (T_m = 54.7 °C), respectively. The mutated Cyt*c* cDNA sequences were subcloned into the pLW01 bacterial expression plasmid after restriction digestion with NcoI and BamHI. Note that the Cyt*c* cDNA contains an internal NcoI restriction site; thus, the fragments were first fully digested with BamHI following partial (3-min) digestion with NcoI and purification of the correct size fragment after agarose gel electrophoresis. Constructs were confirmed by sequencing and used to transform competent *E. coli* C41 (DE3) cells for protein overexpression (10). The clones were inoculated into 20 ml of TB medium (Difco) containing 100 μg/ml carbenicillin and grown overnight at 37 °C under shaking. These cultures were used to inoculate 4 liters of 100 μg/ml carbenicillin-containing TB medium and were grown until an A_{600} of 2–3 was reached. At this time, the expression of cytochrome *c* was induced by the addition of 100 μM isopropyl β-D-1-thiogalactopyranoside, and the protein was overexpressed for 6 h at 37 °C. The cells were harvested by centrifugation for 40 min at 8,400 × *g*, 4 °C, and the pellets were immediately stored at −80 °C until used for Cyt*c* extraction. The bacterial pellets were resuspended in lysis buffer containing 20 mM phosphate buffer, pH 7.4, supplemented with a protease inhibitor mixture (P8340, Sigma) as recommended by the manufacturer. For every 10 g of bacterial pellet, 100 ml of lysis buffer were used, and the resuspended cells were lysed using a French pressure cell press (AMINCO, American Instrument Co.). The lysates were centrifuged at 15,000 rpm for 45 min, the pH of the supernatant was adjusted to 7.4, and Cyt*c* variants were purified by ion exchange chromatography as described above for kidney Cyt*c* isolation. For expression of Cyt*c* variants in Cyt*c* double knock-out mouse lung fibroblasts (15), the pBABE-puro expression plasmid (Addgene, Cambridge, MA) was used. A similar PCR mutagenesis approach was performed as above, and fragments were cloned into the BamHI and EcoRI restriction sites using the following primers: outer forward primer pBABE, 5′-ATCTTGTGGAAAGGACGCGGGATCCATGGGTGATGTTGAAAAA-3′ (T_m = 68.0 °C); outer reverse primer pBABE, 5′-GGTCGACCACTGTGCTGGCGAATTCTTACTTATCGTCGTCATCCTTGTAATCTTCATTAGTAGCC-3′ (T_m = 68.8 °C). The resultant C-terminal 1×FLAG-tagged wild-type, T28E phosphomimetic mutant, and T28A non-phosphorylatable mutant constructs were transfected into Cyt*c* double knock-out lung fibroblast cells and cultured in DMEM (high glucose, Gibco BRL), supplemented with 10% fetal bovine serum, 1,000 units of penicillin/streptomycin, 1 mM pyruvate, 50 μg/ml uridine at 37 °C and 5% CO_2. Stable cell lines expressing the three Cyt*c* variants as well as an empty vector control cell line were selected in the presence of 4 μg/ml puromycin.

CD Spectroscopy—CD spectra of cytochrome *c* variants (wild type, T28A, T28E, and bovine heart cytochrome *c* (Sigma)) were recorded on a Jasco J-815 spectrometer using a 0.6-mm path length quartz cuvette. Proteins were diluted to 220 μM final concentration in 100 mM phosphate buffer, pH 7.4, and 1 ml of protein solution was reduced with 250 μM ascorbate. An average of three scans were collected at 20 °C at a resolution of 1 nm.

Crystallization of WT, T28A, and T28E Cytochrome c and Data Analysis—Cyt*c* was gel-filtered on a S100 column to reduce aggregates and concentrated to ≥15 mg/ml in water. To establish a defined oxidation state, the proteins were oxidized with 5 mM $K_3Fe(CN)_6$ before crystallization. Crystals were grown by vapor diffusion after mixing 1 μl of protein solution with 1 μl of precipitant solution and equilibrating the drop against 0.5 ml of the precipitant at room temperature. The respective precipitant solutions for crystals of the WT, T28A, and T28E Cyt*c* are listed in supplemental Table 1. Crystals usually appeared within 1 week. Crystals were soaked for 10 min in a cryo-protectant solution (supplemental Table 1) before flash freezing in liquid nitrogen. Single crystal diffraction data were collected at the Life Sciences Collaborative Access Team facility (Advanced Photon Source sector 21, Argonne National Laboratory). The data were collected over a full 360° rotation in either 0.6 or 1.0° frames and integrated using XDS (42) in AutoProc (43). For structure solution and refinement, the native data set was solved using chain A of the human Y48F Cyt*c* structure (PDB entry 3ZOO) (44) in PHENIX (45). It was refit with AutoBuild in the PHENIX suite and refined with PHENIX initially to obtain occupancies for the FC6 molecules. The refinement was completed to an R_{free} of 0.159 at 1.12 Å resolution with REFMAC5 (46) in CCP4 using refinement parameters and weights optimized with PDB_REDO (47). In particular, PDB_REDO recommended anisotropic temperature factors based on the Hamilton ratio test for all three structures. Electron density was analyzed with COOT (48) in the CCP4 suite of crystallographic programs (49). The FC6 ligands were located and placed in an anomalous diffraction difference map with COOT. Using the WT structure as an example, the highest eight peaks (in order) in the map, are the four heme iron atoms, followed by FC6 202/C, FC6 202/B, FC6 202b/A, and FC6 203b/B. The next three peaks are for three sulfur atoms (Cys[14]/A, Cys[17]/B, Met[80]/D) followed by FC6 202a/A and FC6 202a/B. The last two FC6 positions were included because they had sufficient $2F_o - F_c$ density to fit several of their cyanide groups. The WT structure (PDB entry 5C0Z; 1.12 Å; R_{free} =

0.159) was then used to solve, refit, and refine the structures of the T28A (PDB entry 5C9M) and T28E (PDB entry 5DF5) mutants at 1.36 Å (R_{free} = 0.170) and 1.30 Å (R_{free} = 0.178) resolution, respectively.

Molecular Dynamics and ESP Calculations—Molecular dynamics were performed with YASARA (50) using its conservative "slow" protocol and the recommended default force field, AMBER 2003 (51). The RMSF and average structures plotted in Fig. 3 were calculated with default scripts in the YASARA library. ESPs *in vacuo* were calculated with YASARA to highlight the charge distribution using the recommended NOVA force field (52) and the particle mesh Ewald algorithm (53). The rectangular simulation cell for the ESP calculations was 15 Å from all atoms in the tetramer. No ligands were included in the calculation. Molecular images including the superpositions were calculated in YASARA (50). Plots were generated with Excel using data imported from YASARA. The three electron density plots in Fig. 3 were assembled with PyMOL (version 1.8; Schrödinger, LLC, New York) using electron density calculated by COOT. The final assembly of all figures was done in Photoshop.

Measurement of Cytc Redox Potential—The midpoint redox potential ($E^{0\prime}$) was analyzed spectrophotometrically as described (10) using 2,6-dichloroindophenol (DCIP, $E^{0\prime}$ = 237 mV) as a reference compound, which has an absorption band at 600 nm in its oxidized state. One ml of Cyt*c* solution (2 mg/ml) was mixed in a spectrophotometric cuvette with 2 ml of 50 mM citrate buffer, pH 6.5, 0.1 ml of 1 mM DCIP, and 50 μl of 1 mM $K_3Fe(CN)_6$ to fully oxidize Cyt*c*. Absorbances corresponding to fully oxidized Cyt*c* (A_{550}–A_{570}) and DCIP (A_{600}) were recorded using a Jasco V-570 double beam spectrophotometer. The mixture was then sequentially reduced by 1-μl additions of 5 mM ascorbate (pH 6.5), and absorbance values were acquired at each step. When readings became constant, a few grains of sodium dithionite ($Na_2S_2O_4$) were added to fully reduce Cyt*c* and DCIP. For each step, ratios of oxidized and reduced forms of both compounds were calculated. Data obtained were plotted as $\log(DCIP_{OX}/DCIP_{RED})$ *versus* $\log(Cyt_{OX}/Cyt_{RED})$, yielding a linear graph with a slope of *n*-DCIP/*n*-Cyt*c* and a *y* axis intercept of *n*-Cyt*c*/59.2(*E* Cyt*c* − *E* DCIP). These values were used to calculate the $E^{0\prime}$ (mV) of Cyt*c* from the Nernst equation.

CcO Activity Measurements—Briefly, an aliquot of regulatory competent bovine liver C*c*O, which has the same isozyme complement as kidney C*c*O, was diluted to 3 μM final concentration in the presence of a 40-fold molar excess of cardiolipin and 0.2 mM ATP in C*c*O measuring buffer (10 mM K-HEPES (pH 7.4), 40 mM KCl, 1% Tween 20) and dialyzed overnight at 4 °C to remove cholate bound to C*c*O during enzyme purification. Respiration of C*c*O (150 nM) was analyzed in a closed chamber equipped with a micro-Clark-type oxygen electrode (Oxygraph system, Hansatech, Pentney, UK) at 25 °C in 220 μl of C*c*O measuring buffer and 20 mM ascorbate as electron donor. Increasing amounts of purified Cyt*c* variants (0–25 μM) were added, and oxygen consumption was recorded and analyzed with the Oxygraph software (Hansatech). C*c*O activity was expressed as turnover number (s^{-1}).

Caspase-3 Activation by Cytc Variants—Caspase-3 activity was assessed *in vitro* with cytoplasmic extracts of a mouse lung fibroblast cell line lacking both the somatic and testis-specific Cyt*c* genes (15) as described (10). Briefly, cells from eight 150-mm plates were collected by centrifugation at 4 °C. The pellet was washed once in 5 ml of ice-cold cytosol extraction buffer (20 mM HEPES, pH 7.5, 10 mM KCl, 1.5 mM $MgCl_2$, 1 mM EDTA, 1 mM EGTA, 1 mM dithiothreitol, 1 mM PMSF), resuspended gently in the same buffer, and immediately transferred to an ice-cold Dounce homogenizer. After 15 min of swelling on ice, cells were then broken open with a B-type glass pestle, and cell breakage was confirmed using a microscope. The lysates were transferred to microcentrifuge tubes and centrifuged at 4 °C and 15,000 × *g* for 15 min to remove nuclei and other debris. The protein concentration of the cytosolic fraction-containing supernatant was measured using the DC assay kit (Bio-Rad), and cytosolic extracts were diluted to 2 mg/ml. The EnzChek caspase-3 assay kit (Invitrogen) with rhodamine 110-linked DEVD tetrapeptide, an artificial substrate for caspase-3 that fluoresces upon cleavage, was used. Cytosolic extracts from Cyt*c* double knock-out lung fibroblast cells (2 mg/ml concentration) were incubated with the Cyt*c* variants (15 μg/ml) for 2.5 h at 37 °C. Caspase-3 activity was assessed in the presence or absence of the caspase-3 inhibitor by detection of fluorescence from the cleavage of the artificial caspase-3 substrate over 3 h in 30-min intervals using a Fluoroskan Ascent FL plate reader (Labsystems, Thermo Scientific), 485-nm excitation filter (14-nm bandwidth), and 527-nm emission filter (10-nm bandwidth). The amount of cleaved substrate was calculated from the rhodamine 110 calibration curve, and data were expressed in pmol of cleaved DEVD min^{-1} (mg of protein)$^{-1}$.

Measurement of Rates of Oxidation and Reduction—The kinetics of oxidation of 15 μM ferro-Cyt*c* with 100 μM H_2O_2 and reduction of 15 μM ferri-Cyt*c* with 200 μM ascorbate was measured spectrophotometrically at 550 nm as described (54). Briefly, WT Cyt*c* and T28E and T28A Cyt*c* mutants were reduced with sodium dithionite, and the proteins were separated from the reductant through NAP5 columns. Fifteen μM Cyt*c* in 0.2 M Tris-Cl, pH 7.0, was incubated with 100 μM oxidizing agent H_2O_2, and after 10 s, the decrease of the absorption peak at 550 nm was measured, and the amount of oxidized Cyt*c* was calculated as described above. To measure the kinetics of reduction of Cyt*c* with ascorbate, Cyt*c* variants were fully oxidized with $K_3Fe(CN)_6$ and purified using NAP5 columns. Fifteen μM ferri-Cyt*c* was added to 50 mM sodium phosphate, pH 7.0, and 200 μM ascorbate to a cuvette, which was then sealed from air, and the initial rate of reduction was measured at 550 nm.

Peroxidase Activity of Cytc Mutants—Assessment of peroxidase activity (10) with Amplex Red reagent was performed by measuring the fluorescence of resorufin, an oxidation product of Amplex Red. Cyt*c* (1 μM) was incubated with liposomes containing TOCL/1,2-dioleoyl-*sn*-glycero-3-phosphocholine in a 1:1 ratio for 10 min. The peroxidase reaction was started by the addition of Amplex Red (50 μM) and H_2O_2 (50 μM) and was carried out for 20 min, during which the reaction rate was linear. Fluorescence was detected by employing a "Fusion R" universal microplate analyzer by using an excitation wavelength of 535 nm and an emission wavelength of 585 nm.

Heme Degradation Assay—The degradation of heme was analyzed through dissipation of the Soret band at 408 nm using 5 μM ferri-Cyt*c* from in 50 mM phosphate buffer, pH 6.1, with 3 mM H_2O_2 as described (54). Spectra were scanned initially after 60 s, followed by measurements every 200 s.

In Vitro Phosphorylation of Cytochrome c with AMP Kinase—Cow heart Cyt*c* (300 pmol; Sigma) was incubated with 3 pmol of AMPK (AMPK α1/β1/γ1, Active SignalChem, P47-10H) at 37 °C for 5 or 30 min in the presence and absence of AMP (125 μM) in 25 mM MOPS (pH 7.2), 12.5 mM β-glycerophosphate, 25 mM $MgCl_2$, 2 mM EDTA, 0.25 mM DTT, and 1 mM ATP. Samples were analyzed by Western blotting and mass spectrometry.

Tissue Treatments with AMPK Activator A769662 and Inhibitor Compound C and Western Blotting Analyses—Fresh mouse kidneys were placed in ice-cold ST buffer containing 250 mM sucrose, 20 mM Tris, pH 7.4, 10 mM KF, 1 mM PMSF, 1 mM sodium orthovanadate, supplemented with protease inhibitor mixture (Sigma) and phosphatase inhibitor mixtures 2 (P5726, Sigma) and 3 (P0044, Sigma) according to the manufacturer's protocol. Kidneys were immediately minced with scissors on an ice-cold glass plate, and equal weight (80 mg) was placed in tubes containing 2 ml of buffer following treatment with either 500 μM A769662 (AMPK activator, Tocris, 3336), 3 μM Compound C (AMPK inhibitor, Sigma, P5499), or DMSO (solvent control) for 1 h at 37 °C under shaking. Tubes were put on ice, tissues were pelleted by centrifugation, and buffer was replaced with 1 ml of homogenization buffer (50 mM Tris-Cl, pH 7.5, 1 mM EGTA, 1% Triton-X 100, 1 mM sodium orthovanadate, 50 mM KF, 5 mM sodium pyrophosphate, 0.27 M sucrose, 0.1% β-mercaptoethanol, supplemented with protease inhibitors and phosphatase inhibitor mixtures as above) and homogenized using a Teflon Dounce homogenizer by applying 60 strokes. Homogenates were centrifuged at 22,000 × *g* at 4 °C for 30 min, and supernatants' total protein levels were quantitated using the DC protein assay kit (Bio-Rad). Twenty μg of tissue homogenates were loaded for immunoblotting analyses to check for total and phospho-AMPK levels and phosphoacetyl-CoA carboxylase levels (AMPKα1/2 antibody (H-300), sc-25792; phospho-AMPKα1/2 antibody (Thr^{172}), sc-33524, Santa Cruz Biotechnology; *p*-acetyl-CoA carboxylase (Ser^{79}) antibody 3661, Cell Signaling Technology (Danvers, MA); antibody dilution 1:1,000). Subsequently, 1 mg of homogenate was used for overnight immunoprecipitation of Cyt*c*. A 10% Tris-Tricine-SDS-PAGE was run to analyze total and phospho-AMPK levels, phospho-ACC levels, and threonine phosphorylation of immunoprecipitated Cyt*c* (using a 1:250 dilution of a set of three individual monoclonal anti-phosphothreonine antibodies (1E11, 4D11, and 14B3), EMD Biosciences). In addition, AMPK was immunoprecipitated from kidney homogenates after treatment with 500 μM A769662 for 1 h to analyze Cyt*c* co-immunoprecipitation.

Measurement of Mitochondrial Oxygen Consumption Rate of Tissue Homogenates—Respiration of intact mitochondria in tissue homogenates was determined as described (55), using freshly harvested kidney tissues, following treatment with AMPK activator and inhibitor as above after homogenization in homogenization buffer with 10 strokes. The protein concentration was determined using the DC protein assay kit (Bio-Rad), and diluted to 0.2 mg/ml with KCl buffer (80 mM KCl, 10 mM Tris-HCl, 3 mM MgCl, 1 mM EDTA, 5 mM potassium phosphate, 2.5 mM malate, 0.5 mg/ml BSA, pH 7.4). Mitochondrial respiration was measured at 30 °C using a Clark-type oxygen electrode as described above.

Sucrose Density Gradient Isolation of Mitochondria and Subfractionation—Lung fibroblasts were harvested and resuspended in 10 mM NaCl, 1.5 mM $MgCl_2$, 10 mM Tris-Cl, pH 7.5. They were allowed to swell for 5 min on ice and homogenized using a Teflon-glass homogenizer. The sucrose concentration was adjusted to 250 mM by adding 2 M sucrose and TE buffer (10 mM Tris-Cl, 20 mM EDTA, pH 7.6). The homogenate was centrifuged twice at 1,300 × *g* for 3 min, and the supernatant was collected and centrifuged at 15,000 × *g* for 10 min and washed three times with 250 mM sucrose/TE buffer. The mitochondrial fraction was layered on a discontinuous sucrose gradient containing 1 M sucrose and 1.7 M sucrose in TE buffer. Centrifugation was performed at 70,000 × *g* for 40 min at 4 °C, and mitochondria were retrieved from the interface. Mitochondria were washed in 250 mM sucrose/TE buffer and collected by centrifugation at 22,000 × *g* for 15 min to obtain highly pure mitochondria. The mitochondrial pellet was resuspended in 20 mM sodium phosphate buffer, pH 7.2, 0.02% BSA, and allowed to swell for 20 min on ice, and then 1 mM ATP and 1 mM $MgCl_2$ were added, followed by incubation on ice for 5 min and centrifugation at 15,000 × *g* for 10 min at 4 °C. The supernatant contained the intermembrane space fraction, and the pellet contained mitoplasts, the outer membrane fraction, and the residual intermembrane space fraction.

Isolation and Subfractionation of Mitochondria from Mouse Kidneys—Mouse kidneys were freshly harvested and washed in ice-cold isolation buffer (10 mM Tris, 1 mM EGTA, 200 mM sucrose, pH 7.4 adjusted with MOPS) (56). Kidneys were minced with scissors on an ice-cold glass plate and homogenized with 20 strokes using a Dounce homogenizer on ice. The homogenate was centrifuged at 600 × *g* for 10 min, and the supernatant was centrifuged at 7,000 × *g* for 10 min to pellet mitochondria. The mitochondrial pellet was subfractionated into an intermembrane space fraction and a mitoplast and outer membrane fraction as described above. The fractions were subjected to Western blotting analysis with Cyt*c*, AMPK, phospho-AMPK, and additional control antibodies to demonstrate purity of the fractions.

Measurement of Oxygen Consumption Rate in Intact Cells—Per well, 70,000 cells were cultured in growth medium (DMEM, supplemented with 10% FBS, 1000 units of penicillin/streptomycin, 1 mM pyruvate, and 50 μg/ml uridine) using Seahorse XF^e24 plates. After overnight culture, growth medium was replaced with XF medium, pH 7.4, and intact cell respiration was measured.

ATP Assay—Lung fibroblast cells expressing Cyt*c* variants were scraped and collected and immediately stored at −80 °C until measurement. Release of ATP was performed by boiling after the addition of 300 μl of boiling buffer (100 mM Tris-Cl, pH 7.75, 4 mM EDTA) and immediate transfer of the samples to a boiling water bath for 2 min. Samples were put on ice, sonicated, and diluted 300-fold, and 40 μl of the diluted samples were used to determine the ATP concentration with the ATP

bioluminescence assay kit HS II (Roche Applied Science) according to the manufacturer's protocol. Data were standardized to the protein concentration.

Measurement of $\Delta\Psi_m$—Lung fibroblast cells expressing Cyt*c* variants were grown to 80% confluence. To assess relative changes in $\Delta\Psi_m$, cells were incubated for 30 min in phenol red-free medium containing 1 μM JC-1 (Molecular Probes). JC-1 is able to selectively enter mitochondria, is a monomer at low concentration or at low membrane potential, and emits green fluorescence. At higher membrane potential, JC-1 forms aggregates that emit red fluorescence. Cells were washed with PBS, and fluorescence was measured with an Ascent Fluoroskan plate reader by using an excitation wavelength of 485 nm and an emission wavelength of 590 nm for red aggregates and 527 nm for green monomers.

Mitochondrial ROS Measurement—Cells expressing Cyt*c* variants were cultured in 12-well plates and incubated with 5 μM Mitosox for 30 min in at 37 °C. Cells were washed with PBS, and fluorescence was analyzed with a Synergy H1 plate reader (BioTek, Winooski, VT) by using excitation and emission wavelengths of 510 and 590 nm.

Cell Viability—Cells (100,000 cells/well in 6-well plates) expressing Cyt*c* variants were grown for 48 h and trypsinized, and live cells were counted after staining with trypan blue. For cell viability analyses after treatment with H_2O_2, cell number was doubled, and cells were treated with 50 and 300 μM H_2O_2 for 24 h followed by trypan blue staining.

Statistical Analyses—Statistical analyses were performed using MSTAT version 5.4 (N. Drinkwater, University of Wisconsin) in conjunction with the Wilcoxon rank sum test. Data ($n = 3$–5) are reported as means ± S.D. and were considered statistically significant (*) with $p < 0.05$.

Author Contributions—G. M., Q. J., I. L., J. L., A. A. K., A. Varughese, C. S., and M. H. designed and performed experiments. A. Vaishnav, J. S. B., and B. E. determined the crystal structures. C. T. M., T. H. S., L. I. G., T. L. S., V. E. K., A. R. S., B. F. P. E., and M. H. assisted with the experimental design and supervised the project. G. M. and M. H. wrote the manuscript. All authors edited and approved the final version of the manuscript.

Acknowledgments—This research used resources of the Advanced Photon Source, a United States Department of Energy Office of Science User Facility operated for the Department of Energy Office of Science by Argonne National Laboratory under Contract DE-AC02-06CH11357. Use of the LS-CAT Sector 21 was supported by the Michigan Economic Development Corporation, the Michigan Technology Tri-Corridor (Grant 085P1000817), and Wayne State University Office of the Vice-President for Research.

References

1. Green, D. R., and Reed, J. C. (1998) Mitochondria and apoptosis. *Science* **281,** 1309–1312
2. Kagan, V. E., Tyurin, V. A., Jiang, J., Tyurina, Y. Y., Ritov, V. B., Amoscato, A. A., Osipov, A. N., Belikova, N. A., Kapralov, A. A., Kini, V., Vlasova, I. I., Zhao, Q., Zou, M., Di, P., Svistunenko, D. A., *et al.* (2005) Cytochrome *c* acts as a cardiolipin oxygenase required for release of proapoptotic factors. *Nat. Chem. Biol.* **1,** 223–232
3. Pereverzev, M. O., Vygodina, T. V., Konstantinov, A. A., and Skulachev, V. P. (2003) Cytochrome *c*, an ideal antioxidant. *Biochem. Soc. Trans.* **31,** 1312–1315
4. Chacinska, A., Pfannschmidt, S., Wiedemann, N., Kozjak, V., Sanjuán Szklarz, L. K., Schulze-Specking, A., Truscott, K. N., Guiard, B., Meisinger, C., and Pfanner, N. (2004) Essential role of Mia40 in import and assembly of mitochondrial intermembrane space proteins. *EMBO J.* **23,** 3735–3746
5. Giorgio, M., Migliaccio, E., Orsini, F., Paolucci, D., Moroni, M., Contursi, C., Pelliccia, G., Luzi, L., Minucci, S., Marcaccio, M., Pinton, P., Rizzuto, R., Bernardi, P., Paolucci, F., and Pelicci, P. G. (2005) Electron transfer between cytochrome *c* and p66Shc generates reactive oxygen species that trigger mitochondrial apoptosis. *Cell* **122,** 221–233
6. Goldberg, E., Sberna, D., Wheat, T. E., Urbanski, G. J., and Margoliash, E. (1977) Cytochrome *c*: immunofluorescent localization of the testis-specific form. *Science* **196,** 1010–1012
7. Ferguson-Miller, S., Brautigan, D. L., and Margoliash, E. (1976) Correlation of the kinetics of electron transfer activity of various eukaryotic cytochromes *c* with binding to mitochondrial cytochrome *c* oxidase. *J. Biol. Chem.* **251,** 1104–1115
8. Lee, I., Salomon, A. R., Yu, K., Doan, J. W., Grossman, L. I., and Hüttemann, M. (2006) New prospects for an old enzyme: mammalian cytochrome *c* is tyrosine-phosphorylated *in vivo*. *Biochemistry* **45,** 9121–9128
9. Yu, H., Lee, I., Salomon, A. R., Yu, K., and Hüttemann, M. (2008) Mammalian liver cytochrome *c* is tyrosine-48 phosphorylated *in vivo*, inhibiting mitochondrial respiration. *Biochim. Biophys. Acta* **1777,** 1066–1071
10. Pecina, P., Borisenko, G. G., Belikova, N. A., Tyurina, Y. Y., Pecinova, A., Lee, I., Samhan-Arias, A. K., Przyklenk, K., Kagan, V. E., and Hüttemann, M. (2010) Phosphomimetic substitution of cytochrome *c* tyrosine 48 decreases respiration and binding to cardiolipin and abolishes ability to trigger downstream caspase activation. *Biochemistry* **49,** 6705–6714
11. Kadenbach, B., Arnold, S., Lee, I., and Hüttemann, M. (2004) The possible role of cytochrome *c* oxidase in stress-induced apoptosis and degenerative diseases. *Biochim. Biophys. Acta* **1655,** 400–408
12. Dickerson, L. (2004) Biochemical oxygen demand. in *The Gale Encyclopedia of Science*, 3rd Ed. (Lerner, K. L., and Lerner, B. W., eds) pp. 500–502, Gale Group, Farmington Hills, MI
13. García-Heredia, J. M., Díaz-Quintana, A., Salzano, M., Orzáez, M., Pérez-Payá, E., Teixeira, M., De la Rosa, M. A., and Díaz-Moreno, I. (2011) Tyrosine phosphorylation turns alkaline transition into a biologically relevant process and makes human cytochrome *c* behave as an anti-apoptotic switch. *J. Biol. Inorg. Chem.* **16,** 1155–1168
14. Cammack, R. (1995) Redox States and Potentials. in *Bioenergetics: A Practical Approach* (Brown, G. C., and Cooper, C. E., eds) pp. 93–95, IRL Press, Oxford, UK
15. Vempati, U. D., Diaz, F., Barrientos, A., Narisawa, S., Mian, A. M., Millán, J. L., Boise, L. H., and Moraes, C. T. (2007) Role of cytochrome *c* in apoptosis: increased sensitivity to tumor necrosis factor α is associated with respiratory defects but not with lack of cytochrome *c* release. *Mol. Cell. Biol.* **27,** 1771–1783
16. Kagan, V. E., Bayir, H. A., Belikova, N. A., Kapralov, O., Tyurina, Y. Y., Tyurin, V. A., Jiang, J., Stoyanovsky, D. A., Wipf, P., Kochanek, P. M., Greenberger, J. S., Pitt, B., Shvedova, A. A., and Borisenko, G. (2009) Cytochrome *c*/cardiolipin relations in mitochondria: a kiss of death. *Free Radic. Biol. Med.* **46,** 1439–1453
17. Vempati, U. D., Han, X., and Moraes, C. T. (2009) Lack of cytochrome *c* in mouse fibroblasts disrupts assembly/stability of respiratory complexes I and IV. *J. Biol. Chem.* **284,** 4383–4391
18. Liu, S. S. (1999) Cooperation of a "reactive oxygen cycle" with the Q cycle and the proton cycle in the respiratory chain: superoxide generating and cycling mechanisms in mitochondria. *J. Bioenerg. Biomembr.* **31,** 367–376
19. Obenauer, J. C., Cantley, L. C., and Yaffe, M. B. (2003) Scansite 2.0: Proteome-wide prediction of cell signaling interactions using short sequence motifs. *Nucleic Acids Res.* **31,** 3635–3641
20. Hardie, D. G., Schaffer, B. E., and Brunet, A. (2016) AMPK: an energy-sensing pathway with multiple inputs and outputs. *Trends Cell Biol.* **26,** 190–201
21. Zhao, X., Leon, I. R., Bak, S., Mogensen, M., Wrzesinski, K., Hojlund, K., and Jensen, O. N. (2011) Phosphoproteome analysis of functional mito-

chondria isolated from resting human muscle reveals extensive phosphorylation of inner membrane protein complexes and enzymes. *Mol. Cell. Proteomics* 10.1074/mcp.M110.000299
22. Hopper, R. K., Carroll, S., Aponte, A. M., Johnson, D. T., French, S., Shen, R. F., Witzmann, F. A., Harris, R. A., and Balaban, R. S. (2006) Mitochondrial matrix phosphoproteome: effect of extra mitochondrial calcium. *Biochemistry* **45,** 2524–2536
23. Sanishvili, R., Volz, K. W., Westbrook, E. M., and Margoliash, E. (1995) The low ionic strength crystal structure of horse cytochrome *c* at 2.1 Å resolution and comparison with its high ionic strength counterpart. *Structure* **3,** 707–716
24. Roberts, V. A., and Pique, M. E. (1999) Definition of the interaction domain for cytochrome *c* on cytochrome *c* oxidase. III. Prediction of the docked complex by a complete, systematic search. *J. Biol. Chem.* **274,** 38051–38060
25. Sugitani, R., and Stuchebrukhov, A. A. (2009) Molecular dynamics simulation of water in cytochrome *c* oxidase reveals two water exit pathways and the mechanism of transport. *Biochim. Biophys. Acta* **1787,** 1140–1150
26. Tsukihara, T., Shimokata, K., Katayama, Y., Shimada, H., Muramoto, K., Aoyama, H., Mochizuki, M., Shinzawa-Itoh, K., Yamashita, E., Yao, M., Ishimura, Y., and Yoshikawa, S. (2003) The low-spin heme of cytochrome *c* oxidase as the driving element of the proton-pumping process. *Proc. Natl. Acad. Sci. U.S.A.* **100,** 15304–15309
27. Zhou, M., Li, Y., Hu, Q., Bai, X. C., Huang, W., Yan, C., Scheres, S. H., and Shi, Y. (2015) Atomic structure of the apoptosome: mechanism of cytochrome *c*- and dATP-mediated activation of Apaf-1. *Genes Dev.* **29,** 2349–2361
28. Zaidi, S., Hassan, M. I., Islam, A., and Ahmad, F. (2014) The role of key residues in structure, function, and stability of cytochrome-*c*. *Cell Mol. Life Sci.* **71,** 229–255
29. Guerra-Castellano, A., Díaz-Moreno, I., Velázquez-Campoy, A., De la Rosa, M. A., and Díaz-Quintana, A. (2016) Structural and functional characterization of phosphomimetic mutants of cytochrome *c* at threonine 28 and serine 47. *Biochim. Biophys. Acta* **1857,** 387–395
30. Viollet, B., Athea, Y., Mounier, R., Guigas, B., Zarrinpashneh, E., Horman, S., Lantier, L., Hebrard, S., Devin-Leclerc, J., Beauloye, C., Foretz, M., Andreelli, F., Ventura-Clapier, R., and Bertrand, L. (2009) AMPK: lessons from transgenic and knockout animals. *Front. Biosci.* **14,** 19–44
31. Hardie, D. G. (2014) AMPK–sensing energy while talking to other signaling pathways. *Cell Metab.* **20,** 939–952
32. Dugan, L. L., You, Y. H., Ali, S. S., Diamond-Stanic, M., Miyamoto, S., DeCleves, A. E., Andreyev, A., Quach, T., Ly, S., Shekhtman, G., Nguyen, W., Chepetan, A., Le, T. P., Wang, L., Xu, M., *et al.* (2013) AMPK dysregulation promotes diabetes-related reduction of superoxide and mitochondrial function. *J. Clin. Invest.* **123,** 4888–4899
33. Ix, J. H., and Sharma, K. (2010) Mechanisms linking obesity, chronic kidney disease, and fatty liver disease: the roles of fetuin-A, adiponectin, and AMPK. *J. Am. Soc. Nephrol.* **21,** 406–412
34. Satriano, J., Sharma, K., Blantz, R. C., and Deng, A. (2013) Induction of AMPK activity corrects early pathophysiological alterations in the subtotal nephrectomy model of chronic kidney disease. *Am. J. Physiol. Renal Physiol.* **305,** F727–F733
35. Tong, W. H., Sourbier, C., Kovtunovych, G., Jeong, S. Y., Vira, M., Ghosh, M., Romero, V. V., Sougrat, R., Vaulont, S., Viollet, B., Kim, Y. S., Lee, S., Trepel, J., Srinivasan, R., Bratslavsky, G., *et al.* (2011) The glycolytic shift in fumarate-hydratase-deficient kidney cancer lowers AMPK levels, increases anabolic propensities and lowers cellular iron levels. *Cancer Cell* **20,** 315–327
36. Takiyama, Y., Harumi, T., Watanabe, J., Fujita, Y., Honjo, J., Shimizu, N., Makino, Y., and Haneda, M. (2011) Tubular injury in a rat model of type 2 diabetes is prevented by metformin: a possible role of HIF-1α expression and oxygen metabolism. *Diabetes* **60,** 981–992
37. Zuber, A. M., Centeno, G., Pradervand, S., Nikolaeva, S., Maquelin, L., Cardinaux, L., Bonny, O., and Firsov, D. (2009) Molecular clock is involved in predictive circadian adjustment of renal function. *Proc. Natl. Acad. Sci. U.S.A.* **106,** 16523–16528
38. Firsov, D., and Bonny, O. (2010) Circadian regulation of renal function. *Kidney Int.* **78,** 640–645
39. Hüttemann, M., Lee, I., Grossman, L. I., Doan, J. W., and Sanderson, T. H. (2012) Phosphorylation of mammalian cytochrome *c* and cytochrome *c* oxidase in the regulation of cell destiny: respiration, apoptosis, and human disease. *Adv. Exp. Med. Biol.* **748,** 237–264
40. Lempiäinen, J., Finckenberg, P., Levijoki, J., and Mervaala, E. (2012) AMPK activator AICAR ameliorates ischaemia reperfusion injury in the rat kidney. *Br. J. Pharmacol.* **166,** 1905–1915
41. Sanderson, T. H., Mahapatra, G., Pecina, P., Ji, Q., Yu, K., Sinkler, C., Varughese, A., Kumar, R., Bukowski, M. J., Tousignant, R. N., Salomon, A. R., Lee, I., and Hüttemann, M. (2013) Cytochrome *c* is tyrosine 97 phosphorylated by neuroprotective insulin treatment. *PLoS One* **8,** e78627
42. Kabsch, W. (2010) XDS. *Acta Crystallogr. D Biol. Crystallogr.* **66,** 125–132
43. Vonrhein, C., Flensburg, C., Keller, P., Sharff, A., Smart, O., Paciorek, W., Womack, T., and Bricogne, G. (2011) Data processing and analysis with the autoPROC toolbox. *Acta Crystallogr. D Biol. Crystallogr.* **67,** 293–302
44. Rajagopal, B. S., Edzuma, A. N., Hough, M. A., Blundell, K. L., Kagan, V. E., Kapralov, A. A., Fraser, L. A., Butt, J. N., Silkstone, G. G., Wilson, M. T., Svistunenko, D. A., and Worrall, J. A. (2013) The hydrogen-peroxide-induced radical behaviour in human cytochrome *c*-phospholipid complexes: implications for the enhanced pro-apoptotic activity of the G41S mutant. *Biochem. J.* **456,** 441–452
45. Adams, P. D., Afonine, P. V., Bunkóczi, G., Chen, V. B., Davis, I. W., Echols, N., Headd, J. J., Hung, L.-W., Kapral, G. J., Grosse-Kunstleve, R. W., McCoy, A. J., Moriarty, N. W., Oeffner, R., Read, R. J., Richardson, D. C., Richardson, J. S., Terwilliger, T. C., and Zwart, P. H. (2010) PHENIX: a comprehensive Python-based system for macromolecular structure solution. *Acta Crystallogr. D Biol. Crystallogr.* **66,** 213–221
46. Murshudov, G. N., Skubák, P., Lebedev, A. A., Pannu, N. S., Steiner, R. A., Nicholls, R. A., Winn, M. D., Long, F., and Vagin, A. A. (2011) REFMAC5 for the refinement of macromolecular crystal structures. *Acta Crystallogr. D Biol. Crystallogr.* **67,** 355–367
47. Joosten, R. P., Long, F., Murshudov, G. N., and Perrakis, A. (2014) The PDB_REDO server for macromolecular structure model optimization. *IUCrJ* **1,** 213–220
48. Emsley, P., Lohkamp, B., Scott, W. G., and Cowtan, K. (2010) Features and development of Coot. *Acta Crystallogr. D Biol. Crystallogr.* **66,** 486–501
49. Winn, M. D., Ballard, C. C., Cowtan, K. D., Dodson, E. J., Emsley, P., Evans, P. R., Keegan, R. M., Krissinel, E. B., Leslie, A. G. W., McCoy, A., McNicholas, S. J., Murshudov, G. N., Pannu, N. S., Potterton, E. A., Powell, H. R., *et al.* (2011) Overview of the CCP4 suite and current developments. *Acta Crystallogr. D Biol. Crystallogr.* **67,** 235–242
50. Krieger, E., and Vriend, G. (2015) New ways to boost molecular dynamics simulations. *J. Comput. Chem.* **36,** 996–1007
51. Duan, Y., Wu, C., Chowdhury, S., Lee, M. C., Xiong, G., Zhang, W., Yang, R., Cieplak, P., Luo, R., Lee, T., Caldwell, J., Wang, J., and Kollman, P. (2003) A point-charge force field for molecular mechanics simulations of proteins based on condensed-phase quantum mechanical calculations. *J. Comput. Chem.* **24,** 1999–2012
52. Krieger, E., Koraimann, G., and Vriend, G. (2002) Increasing the precision of comparative models with YASARA NOVA–a self-parameterizing force field. *Proteins* **47,** 393–402
53. Essmann, U., Perera, L., Berkowitz, M. L., Darden, T., Lee, H., and Pedersen, L. G. (1995) A smooth particle mesh Ewald method. *J. Chem. Phys.* **103,** 8577–8593
54. Liu, Z., Lin, H., Ye, S., Liu, Q. Y., Meng, Z., Zhang, C. M., Xia, Y., Margoliash, E., Rao, Z., and Liu, X. J. (2006) Remarkably high activities of testicular cytochrome *c* in destroying reactive oxygen species and in triggering apoptosis. *Proc. Natl. Acad. Sci. U.S.A.* **103,** 8965–8970
55. Pecinová, A., Drahota, Z., Nusková, H., Pecina, P., and Houštěk, J. (2011) Evaluation of basic mitochondrial functions using rat tissue homogenates. *Mitochondrion* **11,** 722–728
56. Frezza, C., Cipolat, S., and Scorrano, L. (2007) Organelle isolation: functional mitochondria from mouse liver, muscle and cultured fibroblasts. *Nat. Protoc.* **2,** 287–295